

# Study of solar brightness profiles in the 18 – 26 GHz frequency range with INAF radio telescopes I: solar radius

M. Marongiu<sup>\*1</sup>, A. Pellizzoni<sup>1</sup>, S. Mulas<sup>1</sup>, S. Righini<sup>2</sup>, R. Nesti<sup>3</sup>, G. Murtas<sup>4</sup>, E. Egron<sup>1</sup>, M. N. Iacolina<sup>5</sup>, A. Melis<sup>1</sup>, G. Valente<sup>5</sup>, G. Serra<sup>5</sup>, S. L. Guglielmino<sup>6</sup>, A. Zanichelli<sup>2</sup>, P. Romano<sup>6</sup>, S. Loru<sup>6</sup>, M. Bachetti<sup>1</sup>, A. Bemporad<sup>7</sup>, F. Buffa<sup>1</sup>, R. Concu<sup>1</sup>, G. L. Deiana<sup>1</sup>, C. Karakotia<sup>2</sup>, A. Ladu<sup>1</sup>, A. Maccaferri<sup>2</sup>, P. Marongiu<sup>1</sup>, M. Messerotti<sup>8,9</sup>, A. Navarrini<sup>1,10</sup>, A. Orfei<sup>2</sup>, P. Ortu<sup>1</sup>, M. Pili<sup>1</sup>, T. Pisanu<sup>1</sup>, G. Pupillo<sup>2</sup>, A. Saba<sup>5</sup>, L. Schirru<sup>1</sup>, C. Tiburzi<sup>1</sup>, and P. Zucca<sup>11</sup>

<sup>1</sup> INAF - Cagliari Astronomical Observatory, Via della Scienza 5, I-09047 Selargius (CA), Italy

<sup>2</sup> INAF - Institute of Radio Astronomy, Via Gobetti 101, I-40129 Bologna, Italy

<sup>3</sup> Istituto Nazionale di Astrofisica (INAF/OAA), Largo Enrico Fermi 5, I-50125 Firenze, Italy

<sup>4</sup> Los Alamos National Laboratory, Bikini Atoll Rd, Los Alamos, NM 87545, USA

<sup>5</sup> ASI - c/o Cagliari Astronomical Observatory, Via della Scienza 5, I-09047 Selargius (CA), Italy

<sup>6</sup> INAF - Catania Astrophysical Observatory, Via Santa Sofia 78, I-95123 Catania, Italy

<sup>7</sup> INAF - Turin Astrophysical Observatory, Via Osservatorio 20, I-10025 Pino Torinese (TO), Italy

<sup>8</sup> INAF - Trieste Astronomical Observatory, Via Giambattista Tiepolo 11, I-34131 Trieste, Italy

<sup>9</sup> Department of Physics, University of Trieste, Via Alfonso Valerio 2, I-34127 Trieste, Italy

<sup>10</sup> NRAO – Central Development Laboratory, 1180 Boxwood Estate Rd, Charlottesville, VA 22903, USA

<sup>11</sup> ASTRON – The Netherlands Institute for Radio Astronomy, Oude Hoogeveensedijk 4, 7991 PD Dwingeloo, The Netherlands

Received November 28, 2023; accepted January 20, 2024

## ABSTRACT

**Context.** The Sun is an extraordinary workbench, from which several fundamental astronomical parameters can be measured with high precision. Among these parameters, the solar radius  $R_{\odot}$  plays an important role in several aspects, such as in evolutionary models. Moreover, it conveys information about the structure of the different layers that compose the solar interior and its atmosphere. Despite the efforts in obtaining accurate measurements of  $R_{\odot}$ , the subject is still debated and measurements are puzzling and/or lacking in many frequency ranges.

**Aims.** We aimed to determine the mean, equatorial, and polar radii of the Sun ( $R_c$ ,  $R_{eq}$ , and  $R_{pol}$ ) in the frequency range 18.1 – 26.1 GHz. We employed single-dish observations from the newly-appointed Medicina "Gavril Grueff" Radio Telescope and the Sardinia Radio Telescope (SRT) throughout 5 years, from 2018 to mid-2023, in the framework of the SunDish project for solar monitoring.

**Methods.** Two methods to calculate the radius at radio frequencies – the half-power and the inflection-point – are considered and compared. To assess the quality of our radius determinations, we also analysed the possible degrading effects of the antenna beam pattern on our solar maps, using two 2D-models (ECB and 2GECB). We carried out a correlation analysis with the evolution of the solar cycle through the calculation of Pearson's correlation coefficient  $\rho$  in the 13-month running means.

**Results.** We obtained several values for the solar radius – ranging between 959 and 994 arcsec – and  $\rho$ , with typical errors of a few arcsec. These values constrain the correlation between the solar radius and the solar activity, and allow us to estimate the level of the Sun prolateness in the centimetric frequency range.

**Conclusions.** Our  $R_{\odot}$  measurements are consistent with values reported in literature, and provide refined estimations in the centimetric range. The results suggest a weak prolateness of the solar limb ( $R_{eq} > R_{pol}$ ), although  $R_{eq}$  and  $R_{pol}$  are statistically compatible within  $3\sigma$  errors. The correlation analysis using the solar images from the Grueff Radio Telescope shows (1) a positive correlation between the solar activity and the temporal variation of  $R_c$  (and  $R_{eq}$ ) at all observing frequencies, and (2) a weak anti-correlation between the temporal variation of  $R_{pol}$  and the solar activity at 25.8 GHz.

**Key words.** Astronomical instrumentation, methods and techniques; Methods: data analysis; The Sun; Sun: radio radiation

## 1. Introduction

The Sun is a mildly-active star with an 11-year activity cycle (Gleissberg 1966), emitting radiation in the whole electromagnetic spectrum, from radio to gamma-ray frequencies (e.g., Aschwanden 2004; Landi Degl'Innocenti 2007). This star is the closest for which highly-precise fundamental astronomical parameters are known. Among these parameters, the solar radius  $R_{\odot}$  – usually normalised to the unit distance (1 AU) – has been the subject of increasingly accurate measurements and investi-

gations (e.g. Gilliland 1981; Vaquero et al. 2016; Rozelot et al. 2018).

The value of  $R_{\odot}$  allows us to obtain several physical information, such as (1) eclipse computations, (2) the prolateness of the solar limb and (3) insights on the structure of the different layers in the solar atmosphere. Moreover, determining the changes in  $R_{\odot}$  provides insights into the physical mechanisms that may be responsible for its variation (e.g., Gilliland 1981; Ribes et al. 1991), enabling a better understanding of (1) the variation of the luminosity and its possible climate effects on the Earth and its environment (e.g., Dansgaard et al. 1975; Stuiver

\* marco.marongiu@inaf.it

1980; Hiremath & Mandi 2004; Chapman et al. 2008; Hiremath et al. 2015), and (2) the structure of the solar interior, and the role of the underlying magnetism (e.g., Emilio et al. 2000; Kilic & Golbasi 2011; Rozelot et al. 2015; Kosovichev & Rozelot 2018). Until a few decades ago, only optical imaging observations of the Sun were available. The canonical value at optical frequencies of the solar photospheric radius  $R_{\odot,opt}$  – accepted by the International Astronomical Union (IAU, Mamajek et al. 2015; Prša et al. 2016) – is  $695.66 \pm 0.14$  Mm (corresponding to  $959.16 \pm 0.19$  arcsec; Haberreiter et al. 2008), and it is widely used in literature. Observations at radio frequencies started in 1950, with the development of different techniques to measure  $R_{\odot}$  in this band (e.g., Coates 1958; Wrixon 1970; Swanson 1973; Pelyushenko & Chernyshev 1983; Costa et al. 1986, 1999; Selhorst et al. 2004; Alissandrakis et al. 2017; Menezes & Valio 2017; Selhorst et al. 2019a,b).

Despite the importance of having an accurate estimate of  $R_{\odot}$ , its measurement is still a matter of debate, especially for the radio band. Discrepancies in the values reported for  $R_{\odot}$  – and their uncertainties, that over time decreased below the arcsec level (e.g., Ribes et al. 1987, 1989; Table 1 in Menezes & Valio 2017) – could be explained as effects, difficult to quantify and/or not fully included in the measurement procedures. These effects arise from (1) employing instruments with different performances (both ground-based and space-based, Gough 2001), in turn characterised by different angular resolutions, (2) different definitions of the solar limb in the intensity profile (e.g., Meftah et al. 2014) and (3) the presence of a particularly-variable phenomenology close to the limb, such as the limb brightening (e.g., Withbroe 1970; Lindsey et al. 1981; Horne et al. 1981; Selhorst et al. 2019b), whose properties are still debated (e.g., Simon & Zirin 1969; Fuerst et al. 1979; Kosugi et al. 1986; Belkora et al. 1992). Limb brightening can provide important information on the temperature gradient of the solar atmosphere (e.g., Vernazza et al. 1981; Fontenla et al. 1993; Selhorst et al. 2005). The presence of the limb brightening – if confirmed – will be crucial for the measurement of  $R_{\odot}$ , especially in the radio domain. Several authors reported limb brightening only in the polar regions of the solar disk – known as polar brightening – at radio frequencies, in particular at 17 GHz (e.g., Shibasaki 1998; Nindos et al. 1999; Selhorst et al. 2003) with the Nobeyama Radioheliograph (NoRH; Nakajima et al. 1994, 1995) and at 100 and 230 GHz (Selhorst et al. 2019b) with the Atacama Large Millimeter/submillimeter Array (ALMA; Brown et al. 2004). The analysis of Selhorst et al. (2003) showed that at 17 GHz the trend of the polar brightening is strongly anti-correlated with solar activity, and Selhorst et al. (2019b) found that at 100 and 230 GHz the intensity of the polar brightening is more pronounced at the southern pole.

The increasingly-accurate value of  $R_{\odot}$  obtained in recent years suggests to analyse the Sun sphericity. This analysis is deemed to be controversial because of the use of different measurement techniques, instrument calibration (if any), frequency domain of measurements, and – for ground-based instruments – atmospheric effects. At extreme-UV (EUV) frequencies ( $\sim 10^{16}$  GHz), using the solar images obtained by the Extreme Ultraviolet Imager (EIT) aboard the Solar and Heliospheric Observatory (SoHO) satellite (Delaboudinière et al. 1995), different authors showed that the equatorial radius  $R_{eq}$  is larger than the polar radius  $R_{pol}$  (Auchere et al. 1998; Giménez de Castro et al. 2007). Recently, the same conclusion was shown by Zhang et al. (2022) at very low radio frequencies (20–80 MHz) using the radio interferometer LOw Frequency ARray (LOFAR; van Haarlem et al. 2013), in accordance with other similar works

(e.g., Ramesh et al. 2006; Mercier & Chambe 2015; Melnik et al. 2018). On the other hand, Menezes et al. (2021) showed a negligible difference between  $R_{eq}$  and  $R_{pol}$ , obtained from observation with the Solar Submillimeter-wave Telescope (SST, Kaufmann et al. 1994) and ALMA at high radio frequencies (100–405 GHz).

The radius dependence on the solar cycle is also a good indicator of the changes that occur in the solar atmosphere, but this dependence is still a subject of debate (e.g., Reis Neto et al. 2003; Kuhn et al. 2004). Anti-correlated variations with other solar cycle indicators, such as sunspots, were found by several authors (e.g., Secchi 1872; Gilliland 1981; Sofia et al. 1983; Wittmann et al. 1993; Laclare et al. 1996; Dziembowski et al. 2001; Egidi et al. 2006; Qu & Xie 2013), whereas other works find the opposite behaviour (e.g., Ulrich & Bertello 1995; Rozelot 1998; Emilio et al. 2000; Delmas & Laclare 2002; Noël 2004; Chapman et al. 2008). Furthermore, other authors (e.g., Neckel 1995; Antia 1998; Kuhn et al. 2004; Bush et al. 2010) report no – or very small – variations in  $R_{\odot}$  correlated with the solar cycle in their observations. At radio frequencies, variations of  $R_{\odot}$  in phase with the solar cycle are reported by several authors (e.g., Bachurin 1983 at 8 GHz and 13 GHz; Selhorst et al. 2019a at 37 GHz; Costa et al. 1999 at 48 GHz). Selhorst et al. (2004) studied the variation of  $R_{\odot}$  at 17 GHz using NoRH maps over a solar cycle (1992–2003), revealing a good positive correlation between the mean radius  $R_c$  and the solar cycle, but an anti-correlation when the polar radius  $R_{pol}$  is considered. This anti-correlation suggests a possible increase of polar brightening during the solar minima. On the other hand, Menezes & Valio (2017) reported a strong anti-correlation between the solar activity and the variation of  $R_{\odot}$  as measured at 212 and 405 GHz, using  $\sim 16600$  solar maps throughout 18 years (from 1999 to 2017), obtained through SST.

Multi-frequency observations – from radio to X-EUV domain – of the Sun suggest a typical relationship between  $R_{\odot}$  and the observing frequency, but today there is no unique theoretical model to reproduce this dependence. Rozelot et al. (2015) showed that this relationship can be modelled by a parabola, with a minimum at around 45 THz. At different radio frequencies, several authors (Menezes & Valio 2017; Menezes et al. 2021) show that  $R_{\odot}$  follows an exponential trend, as the frequency decreases, where the curve seems to get flatter at higher frequencies ( $\gtrsim 200$  GHz). This trend is in contrast with other analyses (e.g., Meftah et al. 2018; Quaglia et al. 2021) that claimed the extreme weakness of the correlation between  $R_{\odot}$  and the observing frequency.

In this complex and continually-evolving landscape of solar science, the present paper focuses on the measures of the solar radius ( $R_c$ , E-W direction  $R_{eq}$ , and N-S direction  $R_{pol}$ ) and its behaviour over time (also with respect to the solar activity). We use single-dish observations performed with the INAF Medicina "Gavril Grueff" Radio Telescope (hereafter Grueff Radio Telescope) and Sardinia Radio Telescope (SRT) from 2018 to mid-2023 in K-band (18.1 – 26.1 GHz) in the frame of the SunDish project (Pellizzoni et al. 2022). Our analysis allows us to enhance the data available in a frequency range – especially at 20 – 25 GHz – characterised by few and often dated radii measurements (e.g., Fuerst et al. 1979; Costa et al. 1986), and to reveal a different behaviour of  $R_{eq}$  and  $R_{pol}$  with respect to the activity level of the Sun. Thanks to this project, the external layers of the solar atmosphere can be deeply analysed in this radio domain, gaining insights into the properties of the corona in terms of temperature and density distributions (Marongiu et al. 2023). The coverage of the entire solar disk with the suitable resolution,

the low noise, the accurate absolute calibration, and the great sensitivity of INAF's radio telescopes make these data crucial for our purpose.

We organise this paper as follows. A brief description of the INAF radio telescopes used in this work, with the relative implementation of the instrumental configurations and the observing techniques adopted for radio-continuum solar imaging is reported in Section 2. The techniques employed for determining  $R_{\odot}$ , and for analysing the role of the antenna beam pattern on our solar maps are described in Section 3. We present our results in Section 4, where we also include an investigation of the correlation between (1) our solar radius time series and the solar activity cycle, and (2) the equatorial and the polar radius time series. After the discussion of our results in Section 5, we give our conclusions in Section 6.

## 2. Observations and data reduction

In this work the solar data set was obtained by single-dish observations, using the INAF single-dish radio telescopes network<sup>1</sup> in the radio K-band (18 – 26 GHz). This network includes the Grueff Radio Telescope (previously-known as the Medicina radio telescope), the Sardinia Radio Telescope (SRT), and the Noto Radio Telescope<sup>2</sup>. The solar data set covers more than 5 years of observations (from 2018 to mid-2023), corresponding to about half a solar cycle. These solar campaigns are a cornerstone of the "SunDish Project" (PI: A. Pellizzoni)<sup>3</sup>, a collaboration between INAF and ASI (Pellizzoni et al. 2019; Plainaki et al. 2020; Pellizzoni et al. 2022) involved in deeply probing the solar atmosphere.

The 32-m Grueff Radio Telescope has been observing the full solar disk almost once a week since February 2018. The instrument is located in Medicina (near Bologna, Italy) at 25 m elevation in the heart of the Po Valley. Among multiple receivers covering the range 1.3 – 26.5 GHz, we observed the Sun through the K-band dual-feed receiver, primarily using 18.3 and 25.8 GHz as central frequencies. The corresponding beam sizes are 2.1 and 1.5 arcmin, respectively (green circles in Fig. 1). The 64-m Sardinia Radio Telescope (SRT) is located on an isolated plateau at 650 m elevation in Sardinia (Italy). Up to date, the solar campaigns with SRT have taken place mostly once a month at primarily 18.8 and 24.7 GHz through a 7 feeds dual polarization K-band receiver (Bolli et al. 2015; Prandoni et al. 2017). This receiver, customised for solar observations (Pellizzoni et al. 2022), is characterised by a beam size of 1.0 and 0.8 arcmin, respectively (green circles, Fig. 2). SRT is presently upgrading its capabilities with new receivers – exploitable also to observe the Sun – operating up to 116 GHz, thanks to the financial support of the Italian Ministry of University and Research in the context of the National Operative Programme (Programma Operativo Nazionale-PON; Govoni et al. 2021)<sup>4</sup>.

In the time frame 2018 – mid-2023, our observations of the Sun in K-band were mostly obtained at Medicina, with a  $\sim 5\%$  of the total number of sessions provided by the larger SRT. In the frequency range 18.1 – 26.1 GHz we obtained an extensive data set of 327 maps. Among this data set, 145 maps were obtained at 18.3 GHz, and 128 maps were obtained at 25.8 GHz. However, due to high atmospheric opacity and occasional instru-

mental failures, some maps ( $\sim 10\%$ ) had to be discarded, thus reducing the final amount to 287 maps. From 2019 to 2021, the need for a manual solar setup for each observation has limited the use of SRT in the frequency range of 18.3 – 25.5 GHz to a few solar sessions/year. This configuration resulted in 19 solar maps: among these maps, 10 were observed at 18.8 GHz, and 7 were observed at 24.7 GHz. 2 maps at 18.8 GHz were discarded as they were acquired under unsuitable weather conditions or were interested by instrumental failures. As shown in Fig. 2, maps with SRT were mainly performed at 18.8 and 24.7 GHz to exploit the best receiver performance and avoid the Radio-Frequency Interference (RFI).

The solar maps are composed by On-The-Fly (OTF) scans (Prandoni et al. 2017), commanded using the DISCOS antenna control system, in Right Ascension (RA, at the lower frequency) and Declination (DEC, at the higher frequency). These maps cover an area of about  $1.3^{\circ} \times 1.3^{\circ}$  in the sky at Medicina (Fig. 1), and  $1.5^{\circ} \times 1.5^{\circ}$  at SRT (Fig. 2). The radio signal is processed with two different back-ends: (1) the full-stokes spectral-polarimeter SARDARA (1.5 GHz theoretical bandwidth, Melis et al. 2018) at SRT, and (2) the Total-power/intensity at the Grueff Radio Telescope<sup>5</sup>, characterised by a theoretical bandwidth of 0.3 GHz. The high dynamic range of SARDARA allows us to detect in the same image the emission coming both from the bright solar disk and the faint tails near the limb. The Supernova Remnant Cas A is selected for the procedure of absolute brightness temperature calibration (for details see Pellizzoni et al. 2022; Mulas et al. 2022). The solar images from the Grueff Radio Telescope and SRT were extracted from the FITS files produced by the INAF solar pipeline SUNPIT (Marongiu et al. 2022). Details about the OTF mapping techniques, the setup configurations used for the receiver and back-end, the observing strategy, and the data processing (RFI rejection, baseline background subtraction, and image production) are available – both for the Grueff Radio Telescope and SRT – in the first solar paper of the SunDish collaboration (Pellizzoni et al. 2022, and references therein). Moreover, the SunDish Archive<sup>6</sup> includes the data set – regularly updated – of the Grueff Radio Telescope and SRT.

## 3. Data analysis

In this work, we analysed and measured the size of the Sun, in order to obtain information on the value of  $R_c$ ,  $R_{eq}$ , and  $R_{pol}$ , and to study the temporal evolution of these radii. For the radius calculations we used a specific procedure, described in Sect. 3.1. To obtain more robust measurements of the solar radii, and to corroborate the presence of the coronal emission – the analysis of which will be described in detail in a further paper (Marongiu et al. 2023) – we also analysed the contribution of the antenna beam pattern on the solar signal (Section 3.2).

### 3.1. Prescription for calculating the solar radius

The measurement of  $R_{\odot}$  at radio frequencies requires an unambiguous definition of the solar limb, a parameter strongly influenced by the instability of the solar atmosphere. These instabilities are characterised by ever-changing small structures – promi-

<sup>5</sup> From July 2021 this radio telescope is also equipped by the SARDARA system (Mulas et al. 2022), characterised by a theoretical bandwidth of 1.2 GHz. The scientific community can use this back-end since the observing semester 2023A.

<sup>6</sup> <https://sites.google.com/inaf.it/sundish/sundish-images-archive/sundish-archive-summary>

<sup>1</sup> <https://www.radiotelesopes.inaf.it>

<sup>2</sup> We did not carry out any solar observations with the Noto radio telescope, since it is currently under maintenance operations.

<sup>3</sup> <https://sites.google.com/inaf.it/sundish>

<sup>4</sup> <https://sites.google.com/a/inaf.it/pon-srt/home>

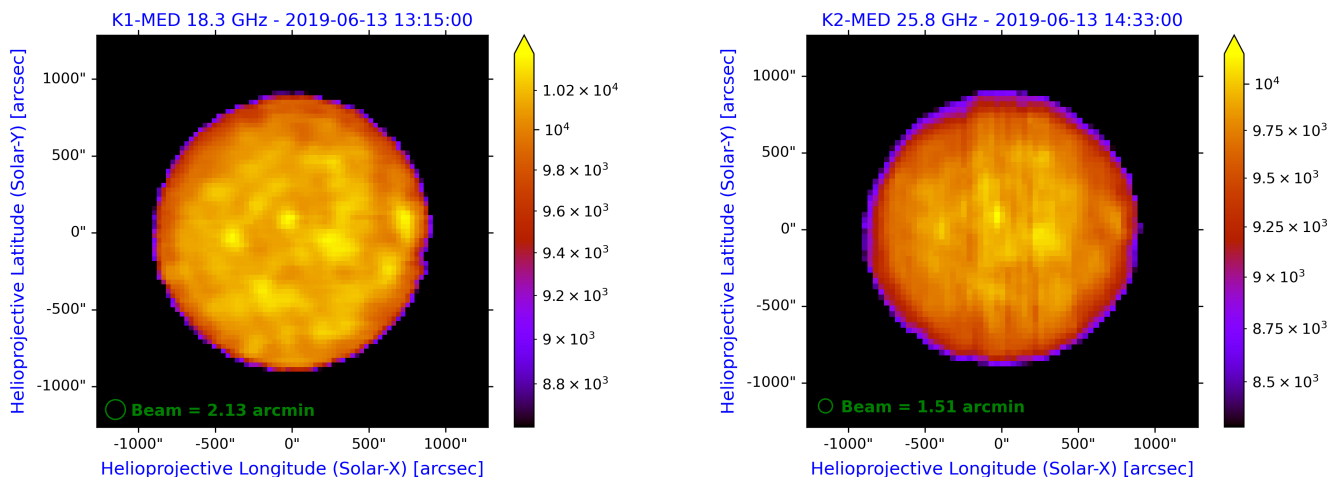


**Fig. 1.** Solar disk image at 18.3 GHz (left) and 25.8 GHz (right) obtained with the Grueff Radio Telescope on June 13<sup>th</sup> 2019, processed with the SUNDARA package (Marongiu et al. 2021). Colorbars indicate  $T_B$  of the solar maps in units of Kelvin. The green circles on the lower left corner of each map mark the Beam Width Half Maximum (BWHM) at the observed frequencies.

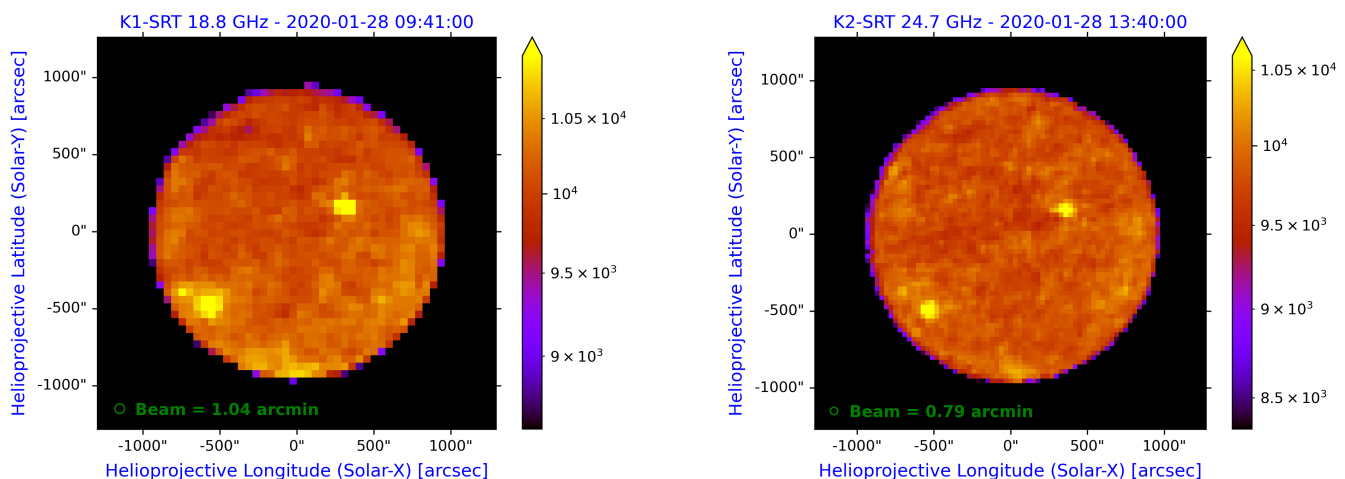


**Fig. 2.** Solar disk image at 18.8 GHz (left) and 24.7 GHz (right) obtained with SRT on January 28<sup>th</sup> 2020, processed with the SUNDARA package (Marongiu et al. 2021). See the caption of Figure 1 for a full description of the colorbars and the symbols.

ment in the observed radio Sun – such as active regions (ARs), sunspots, spicules, and faculae. Two widely-used methods for measuring the radio  $R_\odot$  in the literature are the so-called "half-power method" (hereafter HP-method, Costa et al. 1999; Selhorst et al. 2011; Menezes & Valio 2017; Selhorst et al. 2019a), and the "inflection-point of the limb darkening function" (hereafter IP-method, e.g., Emilio et al. 2012, 2015; Alissandrakis et al. 2017; Menezes et al. 2021). In our analysis both methods are applied and compared.

The HP-method calculates  $R_\odot$  at the points where the brightness temperature  $T_B$  is half of its quiet-Sun Level (QSL)  $T_{qS}$  (Fig. 3, top left), the most common mean temperature in the distribution of the solar disk intensity (for further details, see Landi & Chiuderi Drago 2008; Pellizzoni et al. 2022). In the IP-method, the solar radius is determined by the position of the inflection-point of the solar limb-darkening profile (Fig. 3, top right); this method is less susceptible to the irregularities of the telescope beams and the variations of the  $T_B$  profiles of the Sun, such as the limb-brightening level and the presence of ARs (Menezes et al. 2022).

To determine  $R_\odot$  (with the methods described above) we follow a prescription similar to others described in the literature (Costa et al. 1999; Selhorst et al. 2019a; Menezes & Valio 2017; Menezes et al. 2021, 2022). The first step is the extraction of the solar limb coordinates from each map. These coordinates were determined considering scans, corresponding to brightness profiles (for example, see the green curve in Fig. 3 on top left), in both RA and DEC orientation. During the limb point extraction, some criteria were adopted to avoid extracting limb points associated with ARs, or affected by weather and seasonal effects, instrumental errors, or high atmospheric opacity, which may increase the calculated local radius in that region and hence the average radius (Menezes & Valio 2017; Menezes et al. 2021):

- in the HP-method, we considered only coordinates ranging in a solar ring composed of points with a center-to-limb distance corresponding to a brightness level between  $0.9T_{qS}$  and  $1.1T_{qS}$ ;

- in the IP-method we considered only scans characterised by a signal exceeding the RMS of the solar images<sup>7</sup> ( $\sim 10$  K); the limb coordinates are defined as the maximum and minimum points of the numerical derivative (blue curve in Fig. 3, top right) of each scan across the solar disk.

The second step consists in modelling the solar limb – composed by the limb coordinates extracted in the first step – for each solar map. This limb is modelled following the generic parametric equation of the ellipse:

$$\left[ \frac{X \cos \theta + Y \sin \theta}{R_{eq}} \right]^2 + \left[ \frac{X \sin \theta + Y \cos \theta}{R_{pol}} \right]^2 = 1 \quad (1)$$

where  $\theta$  is the ellipse orientation (set to 0 in this analysis),  $X = x - x_0$  and  $Y = y - y_0$  ( $x_0$  and  $y_0$  are the centre coordinates),  $R_{eq}$  and  $R_{pol}$  indicate the semiaxes of the ellipse. Eq. 1 comes down to the case of the circle, assuming  $R_c = R_{eq} = R_{pol}$ . The modelling is performed using a least-squares method, to determine  $x_0$ ,  $y_0$ , and the solar radii ( $R_c$  in the circular case,  $R_{eq}$  and  $R_{pol}$  in the elliptical case). The calculation of  $R_\odot$  is performed through two alternative approaches:

1. Modelling procedure → the best-fit parameters are obtained from the modelling (Eq. 1 and Fig. 3, bottom left), using either the circle or the ellipse case.
2. Statistical procedure → the radii are obtained through the median values of the centre-to-limb distances, calculated thanks to the distance between each limb point and the fitted centre position (both in the circular and in the elliptical case). The uncertainties in the median values are described by the third and first quartiles of the sample. We calculated three average radii: (a) the average radius  $\bar{R}_{stat}$  considering all the distances, (b) the equatorial radius  $\bar{R}_{eq,stat}$  considering only equatorial latitudes of the solar disk-points between  $30^\circ$  N and  $30^\circ$  S, and (c) the polar radius  $\bar{R}_{pol,stat}$  considering only points above  $60^\circ$  N and below  $60^\circ$  S (Fig. 3, bottom right).

For both approaches, we filtered the final solar limb coordinates thanks to the following iterative process:

- The average radius  $\bar{R}$  is calculated thanks to the distance between each limb point and the fitted centre position. For each fit, the points with centre-to-limb distance (obtained from the modelling) between  $\bar{R} - d$  arcsec and  $\bar{R} + d$  arcsec are considered (where  $d = 10$  arcsec for the circular fit, and  $d = 20$  arcsec for the elliptical fit), and then a new fit is performed with the remaining points. This process is repeated until no other points are discarded.
- If there are less than 25 points remaining, the entire map is discarded, otherwise the radius is calculated. In the case of the statistical procedure, for the calculation of  $R_{eq}$  and  $R_{pol}$  we assume a threshold of 10 remaining points for each side.
- If the standard deviation of the solar limb coordinates is less than 20 arcsec, then the calculated radius is stored and the next map is submitted to this process.

The same method is applied to both INAF radio telescopes, in order to compare these solar radii. The resulting radius values is further normalised at the distance of 1 AU, through the correction for the orbit eccentricity of the Earth. This correction makes the apparent  $R_\odot$  ranging between  $\sim 950$  arcsec (aphelion) and  $\sim 1005$  arcsec (perihelion) during the year.

<sup>7</sup> These scans are characterised by at least a conservative 15% of the pixels with  $T_B \geq 0.15T_{qS}$

To calculate the monthly and annual medians of our calculated  $R_\odot$ , we apply a further criterion, similar to other prescriptions in the literature (e.g., Menezes et al. 2021, 2022). The following criterion reduces the scattering in the distribution of the calculated  $R_\odot$ , caused by maps of low quality (affected by systematic effects of the instrument and/or bad weather conditions).

- For each observing frequency, we calculate the average solar radius  $\bar{R}$ , considering only the values included in the range  $900 - 1050$  arcsec (a conservative range of  $R_\odot$  obtained thanks to our solar observations at K-band).
- With the remaining points (at least 3), we apply the statistical Chauvenet's criterion (Chauvenet 1863; Maples et al. 2018; Konz & Reichart 2023), aimed to extract further outliers from our set of  $R_\odot$ .
- With the remaining points (at least 3), we calculate again  $\bar{R}$ , discarding the values that are outside of the range  $\bar{R} \pm 60$  arcsec.
- We repeat the same step considering the range  $\bar{R} \pm 30$  arcsec.
- Finally, with the remaining points (at least 3), we calculate again  $\bar{R}$ , discarding the values that are outside the more stringent  $\bar{R} \pm 10$  arcsec range. The latter process is repeated until no other points are discarded.

The final value of  $R_\odot$  is the median of the remaining points of the sample, and the uncertainties are described by the third and first quartiles of the sample, respectively.

### 3.2. The role of the antenna beam pattern on the solar maps

One of the most important features that influence the measurement of  $R_\odot$  is the degrading effect of the antenna beam pattern on the solar signal (e.g., Giménez de Castro et al. 2020; Menezes et al. 2022). The analysis of this effect in our solar images allows us to (1) assess the quality of our radius determinations, and (2) reveal the presence of the coronal emission in our maps. In the present work we assess the quality of the radius determinations. The presence of the external coronal emission observed in our solar maps and probing its physical nature (see the tails in the brightness profiles; green line in Fig. 3, top left) is presented in Marongiu et al. (2023). This phenomenology arises from the fact that an observed solar map results from the convolution between the beam radiation pattern of the antenna, hereafter named "beam pattern", and the true solar signal, hereafter named "solar signal" (e.g., Wilson et al. 2013). The solar signal can be obtained from physical and/or empirical models, both using the solar maps (2D-approach) and the extraction of the  $T_B$  profiles as a function of the solar coordinates (1D-approach). We can see an example of these slices of the solar maps in Fig. 3 (green curve, top left). To analyse the effects of the antenna beam pattern on the solar signal, we developed a specific empirical 2D-model based on the convolution between the beam pattern and the solar signal. This 2D modelling procedure requires in input the observed solar map and the beam pattern (both at the same observing frequency for the given radio telescope). In output, it produces the solar signal, whose convolution with the beam pattern results in the observed solar map (the input). This output gives the empirical properties of the solar signal in terms of the size of the solar disk ( $R_{eq}$  and  $R_{pol}$ ), and of the geometrical parameters of the external coronal emission (modelled as a 2D-Gaussian function).

The Grueff and SRT beam patterns were reconstructed using GRASP, a dedicated software for electromagnetic analysis of

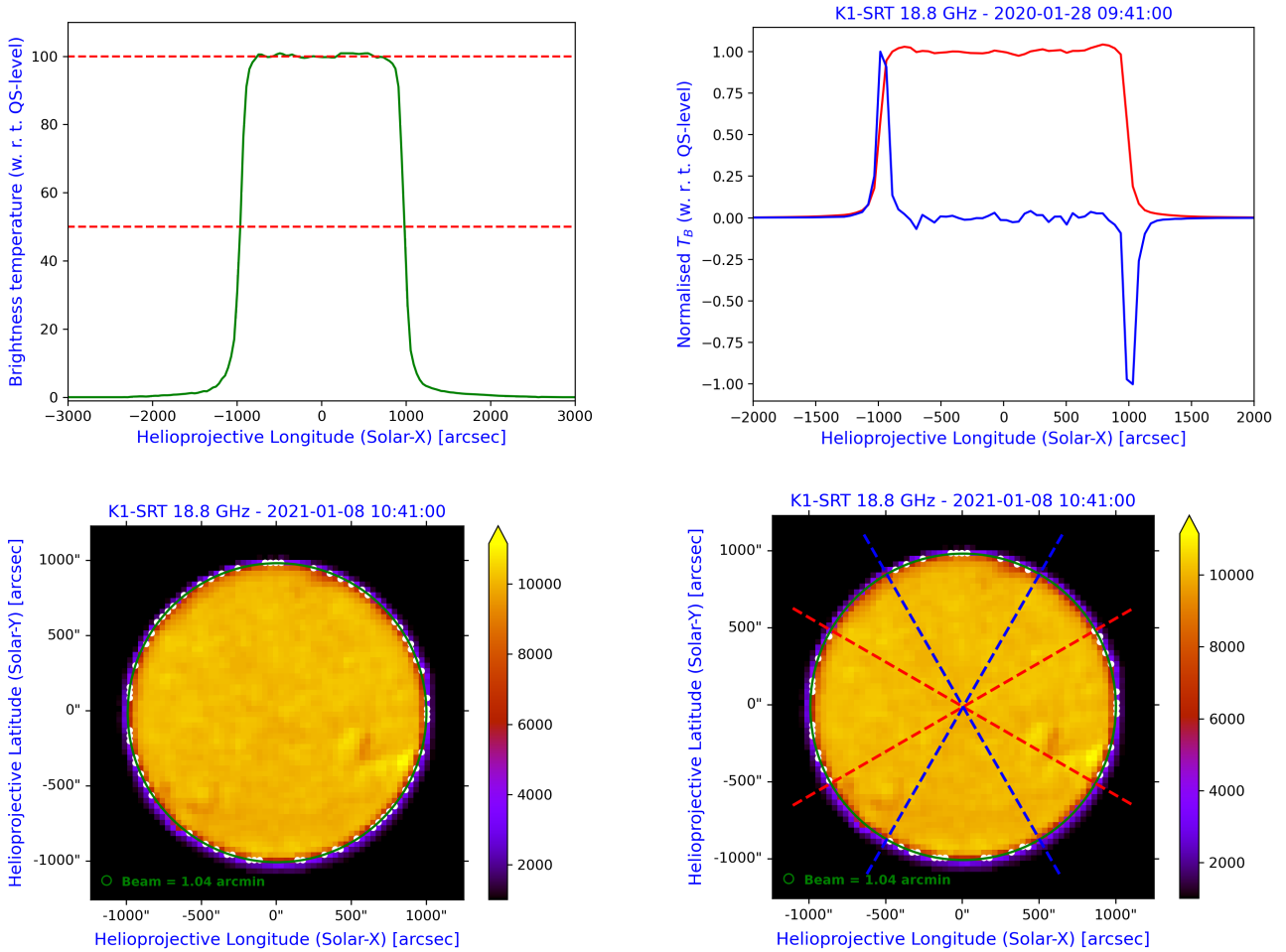


**Fig. 3.** Steps of solar radius measurement: (top left) brightness profile with the  $T_B$  levels (dashed red lines) of  $T_{qS}$  (top line) and the half value of  $T_{qS}$  (bottom line), used in the HP-method; (top right) numerical differentiation of the brightness profile (blue curve), whose minimum and maximum points correspond to the limb coordinates of the equatorial scan (red curve) in the IP-method; (bottom left) limb coordinates (white points) extracted from a solar map with a fit (circle or ellipse, green solid line); (bottom right) limb coordinates (white points) extracted from a solar map with the statistical procedure to estimate  $\bar{R}_{eq,stat}$  and  $\bar{R}_{pol,stat}$  (dashed red and blue lines are the constraints of the equatorial and the polar regions, respectively).

reflector antenna systems integrated into the TICRA Tools software framework<sup>8</sup>. Excluding the measurement noise and the optical residual aberration, the measured beam patterns are in good accordance with the GRASP nominal beam patterns (Prandoni et al. 2017; Egron et al. 2022). As shown in Figs. 4 (for Grueff) and 5 (for SRT), we used four 2D beam patterns (18.3 and 25.8 GHz for Grueff; 18.8 and 24.7 GHz for SRT). We selected these frequencies because they were employed in the vast majority of the solar maps. The single-dish nominal half-power beam width (HPBW) of Grueff and SRT at our observing frequencies ranges between 0.8 and 2.1 arcmin (Sect. 2).

The parametric model of the solar signal is defined as two normalised empirical 2D-models: the Elliptical-based Cylindrical Box (ECB-model), and the Combination between the ECB-model and a 2D-Gaussian function (2GECB-model). The **ECB-model**, tailored only for the solar disk emission of our maps, is defined as:

$$f_b(x, y, R_{eq}, R_{pol}) = \begin{cases} 1 & \text{if } U_b \leq 1 \\ 0 & \text{otherwise} \end{cases} \quad (2)$$

<sup>8</sup> <https://www.ticra.com/software/grasp/>

where  $U_b$  is the elliptical base of the cylindrical box, defined as:

$$U_b(x, y, R_{eq}, R_{pol}) = \left[ \frac{(x - x_C)}{R_{eq}} \right]^2 + \left[ \frac{(y - y_C)}{R_{pol}} \right]^2 \quad (3)$$

where  $x_C$  and  $y_C$  indicate the coordinates of the ellipse center (set to 0, as defined for the solar maps at SRT and Medicina). We used this model as a first approach to the beam pattern analysis.

The solar maps resulting from the ECB-model as the solar signal convolved with the beam pattern, showed that our observed solar maps display an external signal which cannot be explained simply by invoking systematic effects such the smoothing produced by the beam pattern on the solar signal. This aspect is clearly shown in Fig. 6, where the observed limb level of the solar disk (blue dashed line) is higher than the modelled limb level obtained through the ECB-model (red solid line). We will focus on this aspect in a dedicated paper (Marongiu et al. 2023). This incompatibility has led us to consider the **2GECB-model**, tailored both for the solar disk and the external coronal emission (Fig. 7). This model is defined as:

$$f_{bG}(x, y, R_{eq}, R_{pol}, R_{eq,G}, R_{pol,G}, A_G) = \begin{cases} 1 & \text{if } S > 1 \\ S & \text{otherwise} \end{cases} \quad (4)$$

**Table 1.** Measured solar radii at several frequencies in the range 18 – 26 GHz with the Grueff Radio Telescope and SRT radio telescopes, obtained through the modelling described in Sects. 3.1 and 3.2. As specified at 18.3 and 25.8 GHz, we also report the measured values obtained from the averaged solar maps.

| Frequency (GHz) | Telescope | Type radius          | HP-method (arcsec)                    | IP-method (arcsec)                    | ECB-model (arcsec)                    | 2GECB-model (arcsec)                  |
|-----------------|-----------|----------------------|---------------------------------------|---------------------------------------|---------------------------------------|---------------------------------------|
| 18.1            | Grueff    | $R_c$                | 981.8 <sup>+2.0</sup> <sub>-1.0</sub> | 976.7 <sup>+2.9</sup> <sub>-3.4</sub> | -                                     | -                                     |
| 18.1            | Grueff    | $R_{eq}$             | 984.6 <sup>+0.8</sup> <sub>-1.4</sub> | 977.5 <sup>+2.2</sup> <sub>-2.7</sub> | -                                     | -                                     |
| 18.1            | Grueff    | $R_{pol}$            | 980.5 <sup>+2.4</sup> <sub>-3.4</sub> | 976.2 <sup>+2.9</sup> <sub>-2.0</sub> | -                                     | -                                     |
| 18.3            | Grueff    | $R_c$                | 984.7 <sup>+2.6</sup> <sub>-2.1</sub> | 978.7 <sup>+1.7</sup> <sub>-1.9</sub> | -                                     | -                                     |
| 18.3            | Grueff    | $R_{eq}$             | 985.4 <sup>+2.9</sup> <sub>-2.4</sub> | 978.8 <sup>+2.1</sup> <sub>-2.2</sub> | 990.6 <sup>+5.5</sup> <sub>-3.0</sub> | 975.6 <sup>+4.9</sup> <sub>-4.5</sub> |
| 18.3            | Grueff    | $R_{pol}$            | 983.2 <sup>+1.7</sup> <sub>-2.3</sub> | 978.9 <sup>+2.2</sup> <sub>-2.5</sub> | 985.8 <sup>+4.3</sup> <sub>-2.0</sub> | 968.9 <sup>+4.6</sup> <sub>-4.1</sub> |
| 18.3            | Grueff    | $R_c$ (averaged)     | 981.7 ± 0.3                           | 976.4 ± 0.3                           | -                                     | -                                     |
| 18.3            | Grueff    | $R_{eq}$ (averaged)  | 984.9 ± 0.6                           | 977.8 ± 0.8                           | -                                     | -                                     |
| 18.3            | Grueff    | $R_{pol}$ (averaged) | 978.8 ± 0.6                           | 974.0 ± 0.8                           | -                                     | -                                     |
| 18.8            | SRT       | $R_c$                | 978.7 <sup>+0.3</sup> <sub>-0.7</sub> | 974.1 <sup>+1.5</sup> <sub>-0.7</sub> | -                                     | -                                     |
| 18.8            | SRT       | $R_{eq}$             | 979.6 <sup>+0.3</sup> <sub>-0.1</sub> | 974.9 <sup>+1.1</sup> <sub>-2.1</sub> | 981.6 <sup>+0.6</sup> <sub>-1.8</sub> | 973.1 <sup>+1.0</sup> <sub>-3.9</sub> |
| 18.8            | SRT       | $R_{pol}$            | 978.2 <sup>+0.9</sup> <sub>-0.7</sub> | 972.0 <sup>+1.6</sup> <sub>-3.0</sub> | 993.5 <sup>+2.8</sup> <sub>-6.3</sub> | 960.6 <sup>+1.5</sup> <sub>-1.4</sub> |
| 23.6            | Grueff    | $R_c$                | 980.7 <sup>+1.2</sup> <sub>-0.7</sub> | 974.8 <sup>+2.1</sup> <sub>-1.1</sub> | -                                     | -                                     |
| 23.6            | Grueff    | $R_{eq}$             | 979.8 <sup>+1.7</sup> <sub>-1.8</sub> | 974.0 <sup>+0.4</sup> <sub>-0.9</sub> | -                                     | -                                     |
| 23.6            | Grueff    | $R_{pol}$            | 981.4 <sup>+1.3</sup> <sub>-1.4</sub> | 976.2 <sup>+2.7</sup> <sub>-1.5</sub> | -                                     | -                                     |
| 24.7            | SRT       | $R_c$                | 976.7 <sup>+0.5</sup> <sub>-0.9</sub> | 972.4 <sup>+0.1</sup> <sub>-0.6</sub> | -                                     | -                                     |
| 24.7            | SRT       | $R_{eq}$             | 976.0 <sup>+0.7</sup> <sub>-0.2</sub> | 973.7 <sup>+0.2</sup> <sub>-1.8</sub> | 980.3 <sup>+1.4</sup> <sub>-5.8</sub> | 965.1 <sup>+0.2</sup> <sub>-3.0</sub> |
| 24.7            | SRT       | $R_{pol}$            | 976.2 <sup>+1.3</sup> <sub>-0.9</sub> | 972.9 <sup>+0.1</sup> <sub>-1.4</sub> | 982.3 <sup>+5.3</sup> <sub>-1.8</sub> | 959.3 <sup>+6.2</sup> <sub>-7.1</sub> |
| 25.8            | Grueff    | $R_c$                | 982.0 <sup>+1.3</sup> <sub>-1.5</sub> | 975.3 <sup>+1.6</sup> <sub>-2.0</sub> | -                                     | -                                     |
| 25.8            | Grueff    | $R_{eq}$             | 982.2 <sup>+2.3</sup> <sub>-2.0</sub> | 975.1 <sup>+1.9</sup> <sub>-2.2</sub> | 987.3 <sup>+3.7</sup> <sub>-2.9</sub> | 964.2 <sup>+5.8</sup> <sub>-4.4</sub> |
| 25.8            | Grueff    | $R_{pol}$            | 981.2 <sup>+1.4</sup> <sub>-1.3</sub> | 975.5 <sup>+1.2</sup> <sub>-1.7</sub> | 985.2 <sup>+2.1</sup> <sub>-2.9</sub> | 961.1 <sup>+5.6</sup> <sub>-9.5</sub> |
| 25.8            | Grueff    | $R_c$ (averaged)     | 979.3 ± 0.4                           | 972.1 ± 0.4                           | -                                     | -                                     |
| 25.8            | Grueff    | $R_{eq}$ (averaged)  | 979.9 ± 0.9                           | 971.9 ± 0.9                           | -                                     | -                                     |
| 25.8            | Grueff    | $R_{pol}$ (averaged) | 977.9 ± 0.9                           | 973.1 ± 0.9                           | -                                     | -                                     |
| 26.1            | Grueff    | $R_c$                | 981.0 <sup>+0.9</sup> <sub>-1.4</sub> | 973.8 <sup>+1.0</sup> <sub>-0.6</sub> | -                                     | -                                     |
| 26.1            | Grueff    | $R_{eq}$             | 980.6 <sup>+3.2</sup> <sub>-1.4</sub> | 972.4 <sup>+0.6</sup> <sub>-0.6</sub> | -                                     | -                                     |
| 26.1            | Grueff    | $R_{pol}$            | 981.1 <sup>+1.0</sup> <sub>-1.5</sub> | 974.2 <sup>+1.3</sup> <sub>-0.7</sub> | -                                     | -                                     |

where  $R_{eq,G}$  and  $R_{pol,G}$  indicate the  $1\sigma$  standard deviation among the equatorial and polar semi-axis of the 2D-Gaussian function, respectively, and  $A_G$  is the amplitude of the 2D-Gaussian function.  $S$  indicates the sum  $U_b + U_G$ , where  $U_b(x, y, R_{eq,G}, R_{pol,G})$  is defined by Eq. 3, and  $U_G$  indicates the ellipse-shaped 2D-Gaussian function, defined as:

$$U_G(x, y, R_{eq,G}, R_{pol,G}, A_G) = \begin{cases} 1 & \text{if } H > 1 \\ H & \text{otherwise} \end{cases} \quad (5)$$

where  $H = A_G e^{-U_b/2}$ . This model is designed considering (1) both the 2D-Gaussian and the ECB-model centered at  $x_C = y_C = 0$ , and (2) the 2D-Gaussian function defined only outside the ECB-model region. As we describe in Sect. 4 and discuss in Sect. 5.1, the observed solar maps are well fitted with the 2D solar maps obtained through the 2D-model, using our beam pattern and the 2GECB-model as the solar signal.

These 2D-models were developed thanks to a Bayesian approach based on Markov Chain MonteCarlo (MCMC) simulations (e.g. Sharma 2017). For this approach we used the Python `emcee` package<sup>9</sup> (Foreman-Mackey et al. 2013). The model parameters, analysed with `emcee` to flush out degeneracies, are constrained through the definition of prior distributions (uniform in this work) that encode preliminary and general information. The complete uniform prior distribution adopted in our analysis is listed in Table 3. The parameters labelled with 0 indicate

the initial best-fit parameters, calculated through the maximisation of the likelihood function, using the sequential least squares programming tools available in the Python `SciPy` package<sup>10</sup> (Jones et al. 2001–). In the MCMC analysis, the beginning of the ensemble sampler is characterised by an initial period – called “burn-in”, discarded by the analysis – where the convergence of the average likelihood across the chains is unstable (recommended chains: 300). The number of subsequent Markov chains are set up in 1000 steps, with a number of 20 walkers. All the uncertainties are reported at 68% ( $1\sigma$ ).

## 4. Results

We used 304 solar maps (287 with Grueff and 17 with SRT) to calculate the radii, and the correlation between the radii and the solar activity (and between  $R_{eq}$  and  $R_{pol}$ ). We observed at seven central frequencies with Grueff and SRT: 18.1, 18.3, 18.8, 23.6, 24.7, 25.8, and 26.1 GHz. Among these frequencies, for our analysis we selected four frequencies, characterised by a uniform time coverage from 2018 to date: 18.3 and 25.8 GHz for Grueff, 18.8 and 24.7 GHz for SRT. Moreover, for this analysis we also used two averaged solar maps at 18.3 and 25.8 GHz acquired in Medicina during the minimum solar activity (2018–2020). Our data set is composed of solar maps normalised at 1 AU, and we considered only the medium/high-quality maps to

<sup>9</sup> <https://emcee.readthedocs.io/en/stable/>

<sup>10</sup> <http://www.scipy.org/>

**Table 2.** Measured solar radii at several frequencies in the range 18 – 26 GHz with the Grueff and SRT radio telescopes, obtained through the statistical approach described in Sect. 3.1. As specified at 18.3 and 25.8 GHz, we also report the measured values obtained from the averaged solar maps.

| Frequency (GHz) | Telescope | Type radius          | Stat - HP-method<br>Ellipse (arcsec)  | Stat - HP-method<br>Circle (arcsec)   | Stat - IP-method<br>Ellipse (arcsec)  | Stat - IP-method<br>Circle (arcsec)   |
|-----------------|-----------|----------------------|---------------------------------------|---------------------------------------|---------------------------------------|---------------------------------------|
| 18.1            | Grueff    | $R_c$                | 981.8 <sup>+1.5</sup> <sub>-0.9</sub> | 981.8 <sup>+2.0</sup> <sub>-1.0</sub> | 976.7 <sup>+2.4</sup> <sub>-3.2</sub> | 976.6 <sup>+2.9</sup> <sub>-3.4</sub> |
| 18.1            | Grueff    | $R_{eq}$             | 983.8 <sup>+1.4</sup> <sub>-0.8</sub> | 982.6 <sup>+1.4</sup> <sub>-2.0</sub> | 977.3 <sup>+1.7</sup> <sub>-3.1</sub> | 977.3 <sup>+2.5</sup> <sub>-4.5</sub> |
| 18.1            | Grueff    | $R_{pol}$            | 981.2 <sup>+1.2</sup> <sub>-3.4</sub> | 981.5 <sup>+1.9</sup> <sub>-1.5</sub> | 975.9 <sup>+2.2</sup> <sub>-1.9</sub> | 976.4 <sup>+2.4</sup> <sub>-3.6</sub> |
| 18.3            | Grueff    | $R_c$                | 984.1 <sup>+2.2</sup> <sub>-2.1</sub> | 984.6 <sup>+2.6</sup> <sub>-2.1</sub> | 978.6 <sup>+2.1</sup> <sub>-2.6</sub> | 978.6 <sup>+1.7</sup> <sub>-1.9</sub> |
| 18.3            | Grueff    | $R_{eq}$             | 984.2 <sup>+3.1</sup> <sub>-1.7</sub> | 984.5 <sup>+3.2</sup> <sub>-2.0</sub> | 978.2 <sup>+2.2</sup> <sub>-2.2</sub> | 978.3 <sup>+1.9</sup> <sub>-1.9</sub> |
| 18.3            | Grueff    | $R_{pol}$            | 982.9 <sup>+1.8</sup> <sub>-2.1</sub> | 984.2 <sup>+2.2</sup> <sub>-2.3</sub> | 978.1 <sup>+2.0</sup> <sub>-2.6</sub> | 978.2 <sup>+1.9</sup> <sub>-1.3</sub> |
| 18.3            | Grueff    | $R_c$ (averaged)     | 981.4 <sup>+8.3</sup> <sub>-7.2</sub> | 981.3 <sup>+5.7</sup> <sub>-4.7</sub> | 975.6 <sup>+7.0</sup> <sub>-7.0</sub> | 976.4 <sup>+4.0</sup> <sub>-5.0</sub> |
| 18.3            | Grueff    | $R_{eq}$ (averaged)  | 983.7 <sup>+8.5</sup> <sub>-7.8</sub> | 981.0 <sup>+5.6</sup> <sub>-5.3</sub> | 977.2 <sup>+6.7</sup> <sub>-7.5</sub> | 976.8 <sup>+3.7</sup> <sub>-4.0</sub> |
| 18.3            | Grueff    | $R_{pol}$ (averaged) | 978.4 <sup>+8.6</sup> <sub>-6.4</sub> | 980.9 <sup>+6.3</sup> <sub>-3.8</sub> | 974.4 <sup>+5.6</sup> <sub>-6.6</sub> | 975.9 <sup>+4.2</sup> <sub>-4.8</sub> |
| 18.8            | SRT       | $R_c$                | 978.7 <sup>+0.3</sup> <sub>-0.1</sub> | 978.6 <sup>+0.3</sup> <sub>-0.7</sub> | 973.9 <sup>+1.3</sup> <sub>-2.6</sub> | 974.0 <sup>+1.5</sup> <sub>-0.7</sub> |
| 18.8            | SRT       | $R_{eq}$             | 979.4 <sup>+0.3</sup> <sub>-0.5</sub> | 978.6 <sup>+0.5</sup> <sub>-0.2</sub> | 974.4 <sup>+0.8</sup> <sub>-2.2</sub> | 974.3 <sup>+0.8</sup> <sub>-1.5</sub> |
| 18.8            | SRT       | $R_{pol}$            | 978.3 <sup>+1.1</sup> <sub>-1.2</sub> | 978.4 <sup>+0.2</sup> <sub>-0.7</sub> | 972.8 <sup>+1.4</sup> <sub>-3.9</sub> | 973.9 <sup>+1.3</sup> <sub>-1.1</sub> |
| 23.6            | Grueff    | $R_c$                | 980.9 <sup>+0.7</sup> <sub>-1.5</sub> | 980.7 <sup>+1.2</sup> <sub>-0.7</sub> | 975.1 <sup>+1.1</sup> <sub>-1.2</sub> | 974.7 <sup>+2.1</sup> <sub>-1.1</sub> |
| 23.6            | Grueff    | $R_{eq}$             | 980.4 <sup>+0.9</sup> <sub>-2.5</sub> | 980.3 <sup>+1.7</sup> <sub>-0.7</sub> | 973.8 <sup>+1.1</sup> <sub>-0.8</sub> | 975.0 <sup>+1.5</sup> <sub>-1.6</sub> |
| 23.6            | Grueff    | $R_{pol}$            | 981.6 <sup>+0.9</sup> <sub>-1.4</sub> | 980.3 <sup>+2.0</sup> <sub>-0.5</sub> | 975.6 <sup>+2.1</sup> <sub>-1.8</sub> | 976.2 <sup>+0.9</sup> <sub>-2.8</sub> |
| 24.7            | SRT       | $R_c$                | 976.9 <sup>+0.1</sup> <sub>-0.4</sub> | 976.6 <sup>+0.5</sup> <sub>-0.9</sub> | 972.1 <sup>+1.1</sup> <sub>-0.6</sub> | 972.4 <sup>+0.1</sup> <sub>-0.6</sub> |
| 24.7            | SRT       | $R_{eq}$             | 976.6 <sup>+0.9</sup> <sub>-0.4</sub> | 976.0 <sup>+0.7</sup> <sub>-0.1</sub> | 973.6 <sup>+1.4</sup> <sub>-1.4</sub> | 972.1 <sup>+0.5</sup> <sub>-0.3</sub> |
| 24.7            | SRT       | $R_{pol}$            | 977.0 <sup>+0.2</sup> <sub>-1.0</sub> | 976.0 <sup>+1.0</sup> <sub>-0.4</sub> | 972.3 <sup>+0.7</sup> <sub>-0.6</sub> | 971.9 <sup>+0.7</sup> <sub>-0.8</sub> |
| 25.8            | Grueff    | $R_c$                | 981.5 <sup>+1.1</sup> <sub>-1.5</sub> | 982.0 <sup>+1.3</sup> <sub>-1.5</sub> | 975.1 <sup>+1.5</sup> <sub>-1.9</sub> | 975.3 <sup>+1.6</sup> <sub>-2.0</sub> |
| 25.8            | Grueff    | $R_{eq}$             | 982.2 <sup>+1.9</sup> <sub>-2.3</sub> | 981.9 <sup>+1.4</sup> <sub>-1.4</sub> | 974.8 <sup>+1.5</sup> <sub>-1.9</sub> | 975.4 <sup>+1.6</sup> <sub>-2.2</sub> |
| 25.8            | Grueff    | $R_{pol}$            | 980.9 <sup>+1.1</sup> <sub>-1.3</sub> | 981.8 <sup>+1.7</sup> <sub>-1.5</sub> | 975.0 <sup>+1.3</sup> <sub>-1.3</sub> | 975.3 <sup>+2.0</sup> <sub>-1.7</sub> |
| 25.8            | Grueff    | $R_c$ (averaged)     | 978.5 <sup>+8.2</sup> <sub>-6.4</sub> | 978.8 <sup>+5.2</sup> <sub>-3.4</sub> | 971.6 <sup>+7.3</sup> <sub>-5.7</sub> | 972.1 <sup>+3.8</sup> <sub>-4.3</sub> |
| 25.8            | Grueff    | $R_{eq}$ (averaged)  | 978.5 <sup>+6.8</sup> <sub>-5.2</sub> | 979.0 <sup>+5.2</sup> <sub>-2.8</sub> | 969.6 <sup>+6.4</sup> <sub>-5.1</sub> | 971.8 <sup>+3.6</sup> <sub>-4.6</sub> |
| 25.8            | Grueff    | $R_{pol}$ (averaged) | 977.8 <sup>+6.4</sup> <sub>-7.3</sub> | 978.9 <sup>+5.3</sup> <sub>-2.7</sub> | 971.2 <sup>+6.7</sup> <sub>-4.9</sub> | 971.0 <sup>+4.1</sup> <sub>-4.2</sub> |
| 26.1            | Grueff    | $R_c$                | 981.2 <sup>+0.4</sup> <sub>-1.6</sub> | 980.9 <sup>+0.9</sup> <sub>-1.4</sub> | 972.8 <sup>+0.7</sup> <sub>-0.6</sub> | 973.7 <sup>+1.0</sup> <sub>-0.6</sub> |
| 26.1            | Grueff    | $R_{eq}$             | 981.0 <sup>+2.0</sup> <sub>-2.0</sub> | 981.8 <sup>+0.5</sup> <sub>-2.3</sub> | 973.0 <sup>+1.6</sup> <sub>-1.4</sub> | 974.3 <sup>+0.5</sup> <sub>-1.5</sub> |
| 26.1            | Grueff    | $R_{pol}$            | 981.5 <sup>+1.4</sup> <sub>-1.4</sub> | 980.3 <sup>+0.5</sup> <sub>-0.4</sub> | 973.4 <sup>+0.9</sup> <sub>-1.6</sub> | 975.2 <sup>+0.5</sup> <sub>-2.2</sub> |

**Table 3.** Uniform prior distribution adopted for the Bayesian approach in the 2D-models of our analysis.

| Model       | Parameter   | Range   | Unit   |
|-------------|-------------|---|--------|
| ECB-model   | $R_{eq}$    | $R_{eq,0} - 100 \leq R_{eq,0} \leq R_{eq,0} + 100$    | arcsec |
| ECB-model   | $R_{pol}$   | $R_{pol,0} - 100 \leq R_{pol,0} \leq R_{pol,0} + 100$ | arcsec |
| 2GECB-model | $R_{eq}$    | $R_{eq,0} - 100 \leq R_{eq,0} \leq R_{eq,0} + 100$    | arcsec |
| 2GECB-model | $R_{pol}$   | $R_{pol,0} - 100 \leq R_{pol,0} \leq R_{pol,0} + 100$ | arcsec |
| 2GECB-model | $R_{eq,G}$  | $200 \leq R_{eq,G,0} \leq 1200$                       | arcsec |
| 2GECB-model | $R_{pol,G}$ | $200 \leq R_{pol,G,0} \leq 1200$                      | arcsec |
| 2GECB-model | $A_G$       | $0.2 \leq A_{G,0} \leq 10$                            | -      |

avoid systematic and/or meteorological undesired effects. These averaged maps are obtained only from the Grueff Radio Telescope, since the data set obtained with SRT does not uniformly cover our temporal range of observations between 2018 and mid-2023. The discussion of these results is treated in Sect. 5. In this analysis the images were not corrected for center-to-limb variation (CLV) to enhance the visibility of the disk features and show prominences at the same time (e.g., [Alissandrakis et al. 2017](#)).

Our results on the calculation of the median values of  $R_c$ ,  $R_{eq}$ , and  $R_{pol}$  are summarised in Tables 1 and 2 – where the radii are listed by observing frequency, type, and method of calculation – and in Fig. 8. Following the methods described above we obtained values of  $R_\odot$  for the various observing frequencies. Such values range from 959 arcsec (obtained with the 2GECB-

method) and 994 arcsec (obtained with the ECB-method), with typical errors of a few arcsec.

To check for consistency, our results of  $R_c$  are plotted in Figs. 9 (modelling approach) and 10 (statistical approach) with those from other authors at several radio frequencies and different measurement techniques (see [Menezes et al. 2022](#), and Table 1). To guide the eye, an exponential curve (dashed line) is overplotted to show the trend of the radius as a function of the observing frequency, indicating that the radius decreases exponentially at high radio frequencies. Note that the trend curve is just a least-squares exponential fit, not a physical model. Our results are shown by red (Grueff), green (averaged maps of Grueff), and blue points (SRT). These solar radii seem to agree within the uncertainties with the trend, both for the modelling approach and the statistical approach (Figs. 9 and 10). The  $R_\odot$  results (Tables



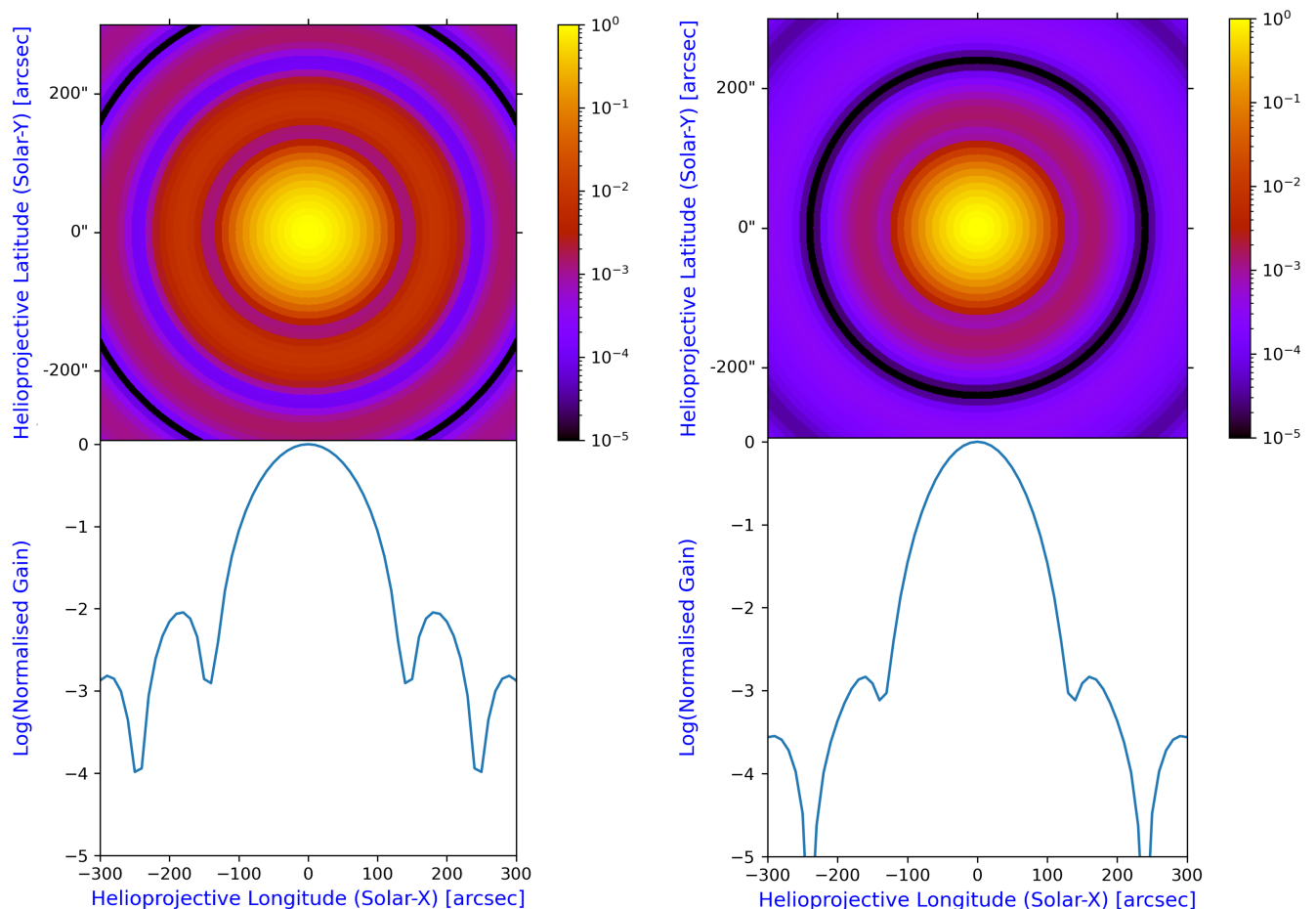


**Fig. 4.** GRASP nominal beam patterns of the Grueff Radio Telescope at 18.3 GHz (left) and at 25.8 GHz (right). (Top) 2D-maps of the beam pattern; (Bottom) 1D-equatorial  $T_B$  profiles of the 2D beam pattern. All the maps are normalised in gain, and shown in logarithmic scale.

1 and 2) indicated that the HP-method yields larger radius values when compared to the IP-method, as already suggested by Menezes et al. (2022) analysing the ALMA and SST data. On average, the values derived from Grueff and SRT maps with the HP-method are  $\sim 5$  arcsec larger than those derived with the IP-method. We note that the results of the average  $R_\odot$  measurements are comparable within  $1\sigma$  error both for the modelling approach and the statistical approach.

Another way to check these radii was to compare them with the 2D-model, considering two different solar signal (ECB-model and 2GECB-model) and the beam patterns of the Grueff Radio Telescope and SRT (Sect. 3.2). Two examples of the application of the 2D-model are shown in Fig. 7. In general, the radii obtained with the 2D-convolution model using the 2GECB-model are at least (1) 7 arcsec smaller than those derived with the HP-method, and (2) 2 arcsec smaller than those derived with the IP-method. A specific comparison with other values obtained in the literature is described in Sect. 5.

To date, the temporal range of our data set is limited with respect to the 11-years solar activity cycle. However, we were able to investigate the temporal evolution of  $R_\odot$  and its relationship with the solar activity. This activity is described through the temporal variation of the sunspot index number, collected by the SILSO data of the Royal Observatory of Belgium (Brussels)<sup>11</sup>. The strength of this relationship is checked through the Pearson’s correlation coefficient (PCC)  $\rho$ . Applying 13-month

**Table 4.** Values of the correlation coefficient  $\rho$  between the solar radius (calculated with the Grueff radio telescope through the HP-method) and the solar activity at radio frequencies characterised by a good temporal coverage. Green values in bold type indicate a strong correlation ( $|\rho| \geq 0.7$ ), black values in bold type indicate a moderate correlation ( $0.3 < |\rho| < 0.7$ ), and the rest indicates a weak correlation ( $|\rho| \leq 0.3$ ).

| Frequency (GHz) | Type correlation    | Modelling     | Statistical (circle) | Statistical (elliptical) | Average $\rho$ |
|-----------------|---------------------|---------------|----------------------|--------------------------|----------------|
| 18.3            | $R_c$ - sunspot     | <b>0.780</b>  | <b>0.779</b>         | <b>0.776</b>             | <b>0.778</b>   |
| 18.3            | $R_{eq}$ - sunspot  | <b>0.913</b>  | <b>0.836</b>         | <b>0.913</b>             | <b>0.887</b>   |
| 18.3            | $R_{pol}$ - sunspot | <b>0.547</b>  | <b>0.786</b>         | <b>0.588</b>             | <b>0.640</b>   |
| 18.3            | $R_{eq} - R_{pol}$  | <b>0.728</b>  | <b>0.979</b>         | <b>0.749</b>             | <b>0.819</b>   |
| 25.8            | $R_c$ - sunspot     | <b>0.761</b>  | <b>0.760</b>         | <b>0.697</b>             | <b>0.739</b>   |
| 25.8            | $R_{eq}$ - sunspot  | <b>0.842</b>  | <b>0.606</b>         | <b>0.848</b>             | <b>0.765</b>   |
| 25.8            | $R_{pol}$ - sunspot | <b>-0.612</b> | <b>0.784</b>         | <b>-0.586</b>            | -0.138         |
| 25.8            | $R_{eq} - R_{pol}$  | <b>-0.677</b> | <b>0.609</b>         | <b>-0.534</b>            | -0.201         |

running means – to avoid the influence of annual modulations (Menezes & Valio 2017; Menezes et al. 2021) – at the solar radii obtained from our maps, we obtain the values of  $\rho$  (Tables 4, 5, and 6; Figs. 11 and 12). We will discuss these results in Sect. 5.2. Future observations with the Grueff Radio Telescope and SRT will expand our data set, resulting in a more exhaustive analysis of this kind of correlation.

<sup>11</sup> <https://www.sidc.be/silso/datafiles>

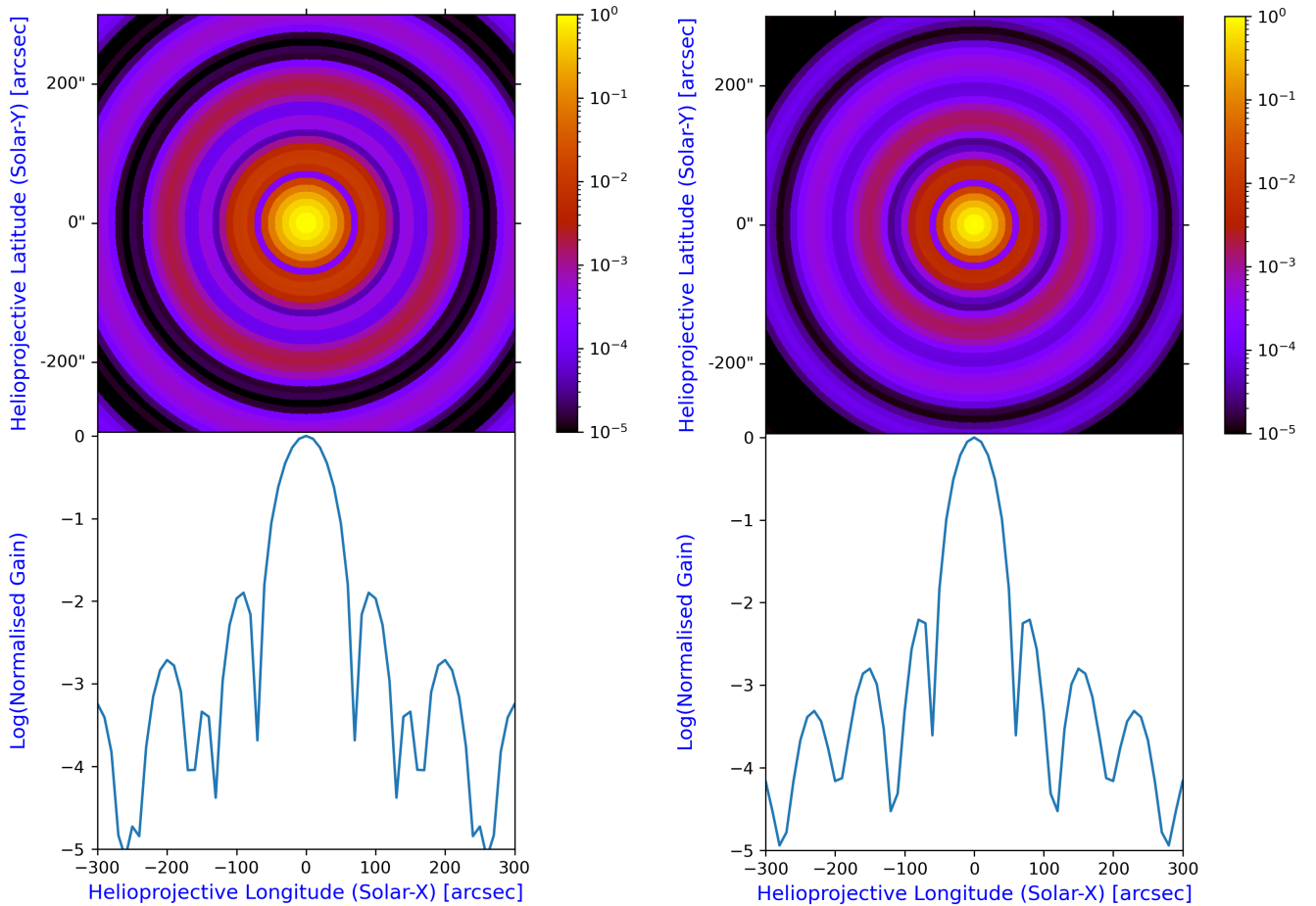


**Fig. 5.** GRASP nominal beam patterns of SRT at 18.8 GHz (left) and at 24.7 GHz (right). (Top) 2D-maps of the beam pattern; (Bottom) 1D-equatorial  $T_B$  profiles of the 2D beam pattern. All the maps are normalised in gain, and shown in logarithmic scale.

**Table 5.** Values of the correlation coefficient  $\rho$  between the solar radius (calculated with the Grueff Radio Telescope through the IP-method) and the solar activity at radio frequencies characterised by a good temporal coverage. See the caption of Table 4 for a full description of the table.

| Frequency (GHz) | Type correlation    | Modelling     | Statistical (circle) | Statistical (elliptical) | Average $\rho$ |
|-----------------|---------------------|---------------|----------------------|--------------------------|----------------|
| 18.3            | $R_c$ - sunspot     | <b>0.649</b>  | <b>0.650</b>         | <b>0.457</b>             | <b>0.585</b>   |
| 18.3            | $R_{eq}$ - sunspot  | <b>0.786</b>  | <b>0.584</b>         | <b>0.622</b>             | <b>0.664</b>   |
| 18.3            | $R_{pol}$ - sunspot | <b>0.444</b>  | <b>0.576</b>         | 0.263                    | <b>0.428</b>   |
| 18.3            | $R_{eq} - R_{pol}$  | <b>0.591</b>  | <b>0.912</b>         | <b>0.599</b>             | <b>0.701</b>   |
| 25.8            | $R_c$ - sunspot     | 0.299         | 0.299                | -0.273                   | 0.108          |
| 25.8            | $R_{eq}$ - sunspot  | 0.121         | <b>0.599</b>         | -0.209                   | 0.170          |
| 25.8            | $R_{pol}$ - sunspot | <b>-0.596</b> | 0.161                | <b>-0.452</b>            | -0.296         |
| 25.8            | $R_{eq} - R_{pol}$  | 0.257         | <b>0.682</b>         | <b>0.588</b>             | <b>0.509</b>   |

**Table 6.** Values of the correlation coefficient  $\rho$  between the solar radius (calculated with the Grueff Radio Telescope) and the solar activity at radio frequencies characterised by a good temporal coverage.  $R_\odot$  is calculated through the ECB- and 2GECB-models described in Sect. 3.2. See the caption of Table 4 for a full description of the table.

| Frequency (GHz) | Type correlation    | $R_\odot$     |               |
|-----------------|---------------------|---------------|---------------|
|                 |                     | ECB           | 2GECB         |
| 18.3            | $R_c$ - sunspot     | –             | –             |
| 18.3            | $R_{eq}$ - sunspot  | <b>0.979</b>  | <b>0.862</b>  |
| 18.3            | $R_{pol}$ - sunspot | 0.212         | <b>-0.785</b> |
| 18.3            | $R_{eq} - R_{pol}$  | 0.253         | -0.330        |
| 25.8            | $R_c$ - sunspot     | –             | –             |
| 25.8            | $R_{eq}$ - sunspot  | <b>0.763</b>  | <b>0.474</b>  |
| 25.8            | $R_{pol}$ - sunspot | 0.167         | <b>-0.747</b> |
| 25.8            | $R_{eq} - R_{pol}$  | <b>-0.419</b> | 0.082         |

## 5. Discussion

### 5.1. Radius calculation

In this work we obtained an accurate measure of the solar radii ( $R_c$ ,  $R_{eq}$ , and  $R_{pol}$ ) in the centimetric range (18.1 – 26.1 GHz) through single-dish observations with the Grueff Radio Telescope and SRT. Our results show a weak prolateness of the solar limb ( $R_{eq} > R_{pol}$ ), although  $R_{eq}$  and  $R_{pol}$  are statistically comparable within  $3\sigma$  errors (Fig. 8). This trend, as discussed by Selhorst et al. (2004), can be explained by variations in the equatorial solar atmosphere during the period of maximum activity that cause an increase in the solar radius at lower latitudes.

We compared the calculation methods (HP, IP, statistical, ECB, 2GECB), showing a variation of the calculated solar ra-

dius based on the used method. By looking at values in Tables 1 and 2, the modelling and the statistical procedures are comparable for the calculation of these mean radii within  $1\sigma$  error. In general, the values of  $R_c$  obtained with the HP-method in the range 18 – 26 GHz are compatible with the other radii obtained in the literature with the same method within a similar frequency range (e.g., Wrixon 1970; Fuerst et al. 1979; Costa et al. 1986; Selhorst et al. 2004, 2011). Small differences could be ascribed to the different angular resolutions of the instruments. At the same observing frequency, a lower resolution translates in values of  $R_\odot$  (and its uncertainty) larger than those obtained with instruments characterised by higher resolution. For example, the value of  $R_c = 976.6 \pm 1.5$  arcsec measured by Selhorst et al.

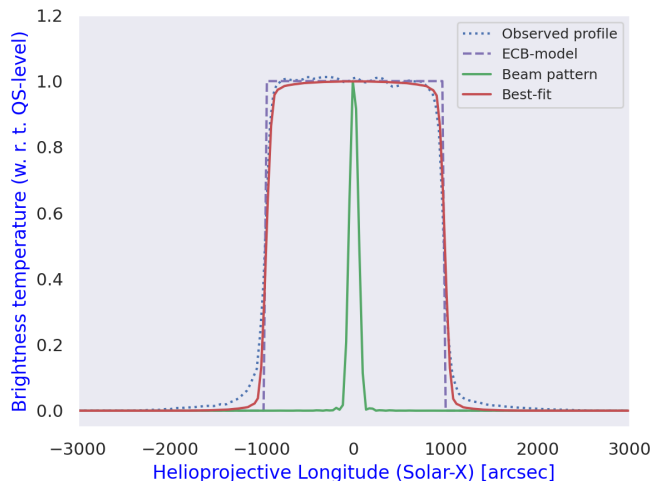


**Fig. 6.** Example of the analysis with the ECB-model using the solar signal in the Grueff Radio Telescope at 18.3 GHz on September 2<sup>nd</sup> 2020. Green solid line indicates the instrumental beam pattern, blue dashed line indicates the observed equatorial  $T_B$  profile of the solar map, violet dotted line indicates the modelled equatorial  $T_B$  profile of the ECB-model (Eq. 3), and red solid line indicates the convolved best-fit  $T_B$  profile using the instrumental beam pattern and the ECB-model as the solar signal.

(2004) at 17 GHz with NoRH (characterised by a spatial resolution of 10 arcsec) is (1) compatible within  $1\sigma$  error to that obtained with SRT ( $\sim 979$  arcsec) at 18.8 GHz, where the beam-size is  $\sim 60$  arcsec, and (2) smaller than that obtained with Grueff ( $\sim 982$  arcsec) at 18.3 GHz, where the beam-size is  $\sim 120$  arcsec, but still within  $2\sigma$  error. Moreover, there are no significant biases arising from image measurement sampling. In our OTF technique, each pixel on solar images is oversampled, since our maps include at least 6 measurements per beam for each subscan (Pellizzoni et al. 2022). A comparison of values obtained with the IP-method is not possible since there are no available measurements in the literature in a frequency range comparable to ours. The available radii are calculated at observing frequencies higher than 100 GHz (e.g. Menezes et al. 2021). The mean radii obtained with the HP-method and the ECB-model – compatible with each other within  $1\sigma$  error – are larger than those obtained with the IP-method and the 2GECB-model. This feature suggests that specific procedures to measure  $R_\odot$ , designed to also describe both the behaviour of the solar disk (such as ARs) and the coronal emission (such as the case of the IP-method and the 2GECB-model), result in a lower bias in solar radius determination (Menezes et al. 2022), and hence in a smaller value of  $R_\odot$ . In particular, the 2D solar maps modelled using our beam pattern and the 2GECB-model as the solar signal (Sect. 3.2), are well fitted with the observed solar map ( $\chi_r^2 \sim 0.8$ ). This modelling is better than that obtained using the ECB-model ( $\chi_r^2 \sim 0.6$ ). Despite the statistically non-significant data set from SRT, from our results (Tables 1 and 2) we preliminarily estimate the possible dependence of the HP- and the IP-methods on the antenna beam pattern, analysing the radii difference caused by these methods. This radii difference follows the same trend (the percentage difference  $\Delta M$  between the radii obtained with the HP-method and the IP-method is  $\sim 0.6\%$ ) both at Grueff and SRT, suggesting that these methods could be independent of the antenna beam pattern. On the other hand, this independence is not strictly defined, since at 25 GHz this trend in the IP-method seems to be

less pronounced ( $\Delta M \sim 0.2\%$ ), suggesting possible dependence on the antenna beam pattern. Future solar sessions at SRT will allow us to clarify this aspect. It is worth noting that approximately 30% of the  $R_\odot$  values ( $\sim 20\%$  of  $R_{eq}$  and  $\sim 40\%$  of  $R_{pol}$ ) obtained with the 2GECB-model – built adopting a Bayesian statistics – are smaller than the canonical and "average" optical solar photospheric radius  $R_{\odot,opt}$  (see Fig. 8, bottom right). However, the peaks of the histogram ( $\sim 973$  arcsec for  $R_{eq}$  and  $\sim 967$  arcsec for  $R_{pol}$ ) are above  $R_{\odot,opt}$  and lower values are considered as statistical fluctuations.

From Fig. 9, we note that our radii are in agreement with the radius-versus-frequency trend of the literature points, where the curve seems to flatten at higher frequencies. That could explain why we obtained similar average values of the radii at our observing frequencies. In this context, it is important to take into account the analysis of Meftah et al. (2018), that claimed the extreme weakness of the correlation between the solar radius and the observing frequency in the visible and the near-infrared, in contrast to the claim made by Rozelot et al. (2015). This weak correlation is even expected due to the sharpness of the solar density profile near the photosphere. Meftah et al. (2018) claimed that the analysis of the possible solar radius dependence on the frequency should be at least based on two different regions of the solar atmosphere (photosphere and chromosphere). This aspect is crucial before fitting any polynomial functions to the measurements.

## 5.2. Time evolution of the solar radius

Despite the irregular and limited coverage both in time and observing frequency of our data set, our investigation at 18.1 – 26.1 GHz about the temporal evolution of the solar radius and its relationship with the solar activity suggests some interesting trends. For this correlation analysis, the SRT data set obtained at 18.8 and 24.7 GHz does not show exhaustive information on the correlation with the solar activity due to the low statistics. Therefore, we used only the data set from Grueff (at 18.3 and 25.8 GHz).

The 13-month running means applied to the solar radii measured at Medicina and the sunspot index number (Tables 4, 5, and 6; Figs. 11 and 12), suggest a strong/moderate positive correlation between the 11-year solar activity cycle and the temporal variation of both  $R_c$  and  $R_{eq}$  at all observing frequencies. Only at 25.8 GHz there is a weak positive correlation obtained with the IP-method. The other cases of correlation show different results according to the approaches for the  $R_\odot$  calculation described in Sects. 3.1 and 3.2. In general, the correlation between  $R_{pol}$  and the solar activity is:

1. weakly/moderately positive at 18.3 GHz with the HP-, IP-, and ECB-methods, and at 25.8 GHz with the ECB-model;
2. weakly negative at 25.8 GHz with the HP- and IP-methods;
3. strongly negative at 18.3 GHz and 25.8 GHz with the 2GECB-model.

Finally, the correlation between  $R_{eq}$  and  $R_{pol}$  is:

1. strongly positive at 18.3 GHz with the HP- and IP-methods;
2. weakly/moderately positive at 25.8 GHz with the IP-method and the 2GECB-model, and at 18.3 GHz with the ECB-model;
3. weakly negative at 18.3 GHz with the 2GECB-model;
4. weakly/moderately negative at 25.8 GHz with the HP-method and the ECB-model.

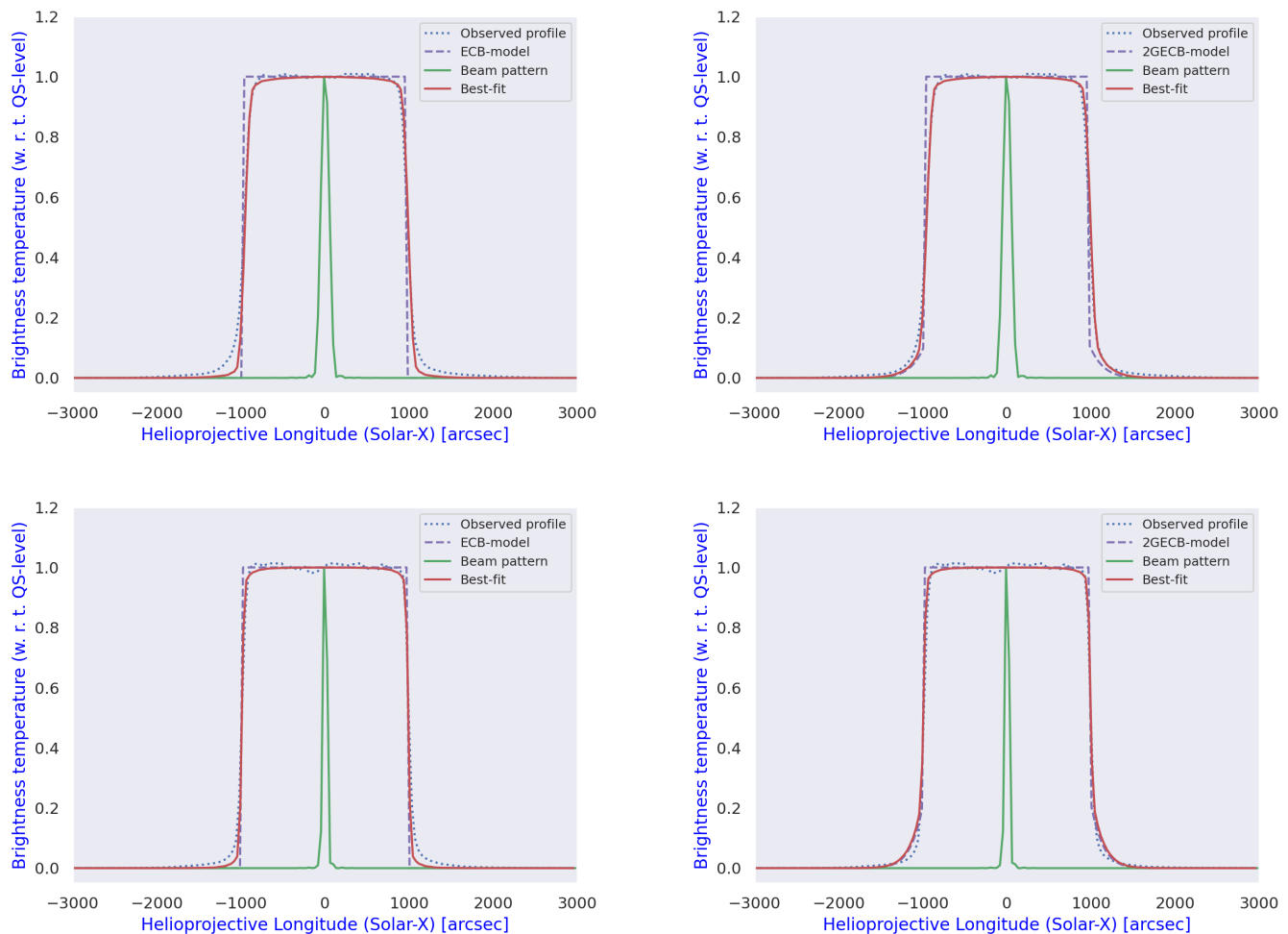


**Fig. 7.** Result of the analysis with the 2D-convolution model, in the context of the equatorial  $T_B$  profile, using the ECB-model (Grueff at 18.3 GHz, top left; SRT at 18.8 GHz, bottom left) and the 2GECB-model (Grueff at 18.3 GHz, top right; SRT at 18.8 GHz, bottom right). The  $T_B$  profiles of the Grueff Radio Telescope are obtained on 6<sup>th</sup> September 2020; the SRT  $T_B$  profiles are obtained on 8<sup>th</sup> January 2021. See the caption of Fig. 6 for a full description of the profiles.

These results suggest that specific procedures to measure  $R_\odot$ , tailored to describe both the behaviour of the solar disk and the coronal emission (such as the case of the IP-method and the 2GECB-model), show a weak/moderate anti-correlation between the temporal variation of  $R_{pol}$  and the solar activity, especially when the 2GECB-model is applied. Among the  $R_\odot$  prescriptions described in this work, the strength of the correlation is inversely proportional to the robustness/complexity of the prescription: for the case of the HP-method, based only on the  $T_B$  level of the brightness profiles, the strength of the correlation is higher than those obtained with more complex prescriptions, such as the ECB-model, IP-method, and the 2GECB-model. In particular, the 2GECB-model is also able to unearth anti-correlation between the temporal variation of  $R_{pol}$  and the solar activity at 18.3 GHz, where generally the thermal emissions from the solar activity – a bias for the radius calculation – are stronger than the counterpart at 25.8 GHz.

Our results of the Medicina "Grueff" Radio Telescope seem to be in agreement with the analyses presented in the literature for similar radio frequencies (Costa et al. 1999; Selhorst et al. 2004, 2011, 2019a), which are expected to be correlated to the solar cycle positively for  $R_c$  and negatively for  $R_{pol}$ . These results are compatible with the presence of correlations between the ra-

dius variations and the solar activity, as suggested by Menezes et al. (2021) monitoring the Sun for more than a solar cycle (from 2007 to 2019) at higher frequencies (212 and 405 GHz) with SST and ALMA facilities. In that work the authors suggest that the  $R_{eq}$  variations are expected to be positively correlated to the solar activity, since the equatorial regions are more affected by the increase of the AR number during solar maxima, making the solar atmosphere warmer in these regions. On the other hand, Menezes et al. (2021) suggest that the anti-correlation between polar radius time series and the solar activity proxies could be explained by a possible increase of the polar limb brightening during solar minima, as also suggested by Selhorst et al. (2004).

Moreover, as shown in Fig. 11, at 18.3 GHz a bump appears at the end of 2020 both in the radii and in the solar activity. This effect seems to corroborate a higher level of the positive correlation between  $R_\odot$  and the solar activity at this observing frequency than 25.8 GHz, in agreement with the conclusions of Menezes et al. (2021) mentioned above about the stronger solar activity in the equatorial regions at the approach of the solar maxima. As we can see in Fig. 12, at 25.8 GHz the time evolution of the 13-month running means applied to the measured solar radii obtained using the ECB- and 2GECB-methods, shows that this bump in the solar activity corresponds to the time when

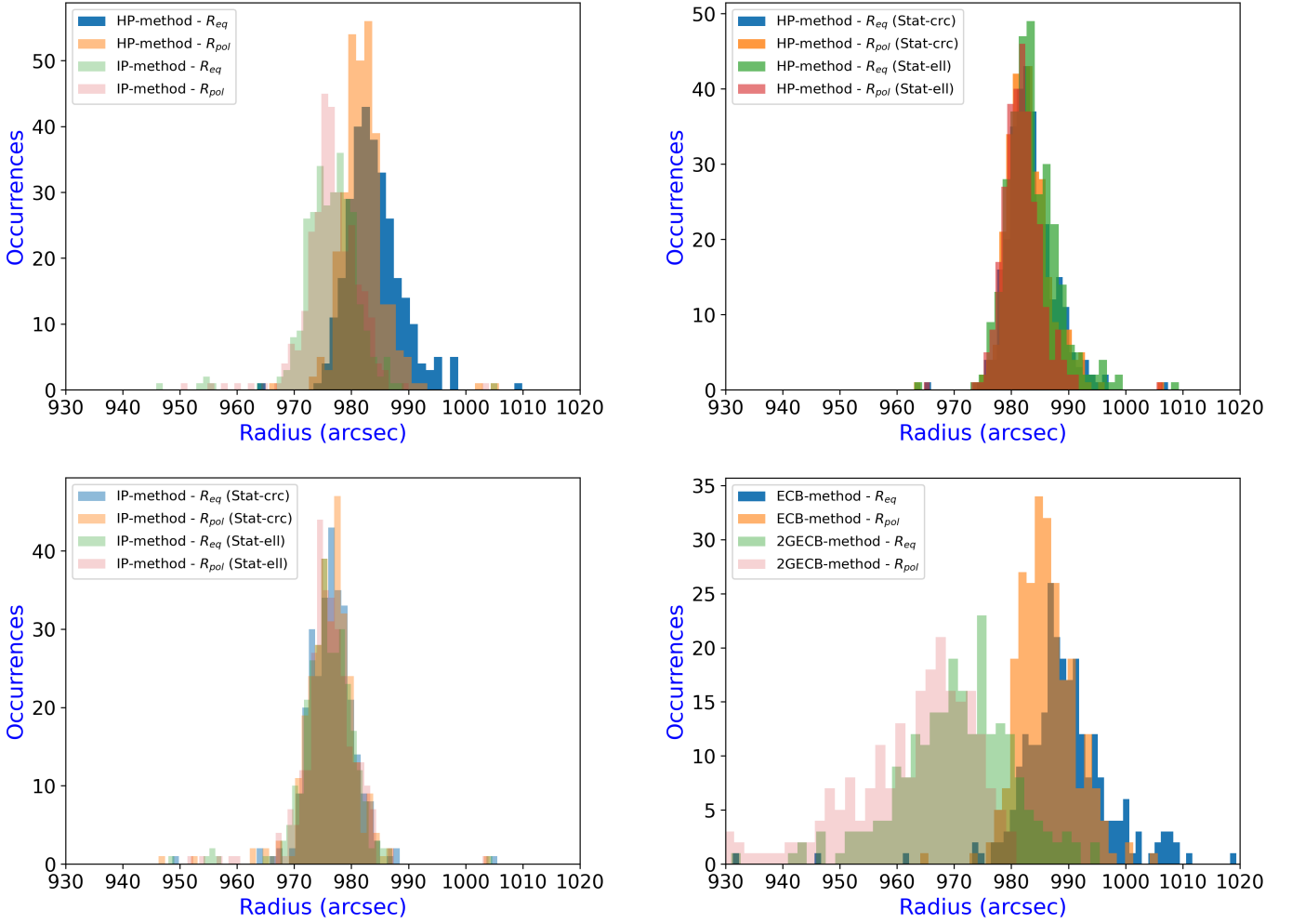


**Fig. 8.** Histograms depicting all the  $R_{eq}$  and  $R_{pol}$  measurements calculated from (top left) the HP- and IP-methods, (top right) the statistical approach using the HP-method, (bottom left) the statistical approach using the IP-method, and (bottom right) the ECB- and 2GECB-methods.

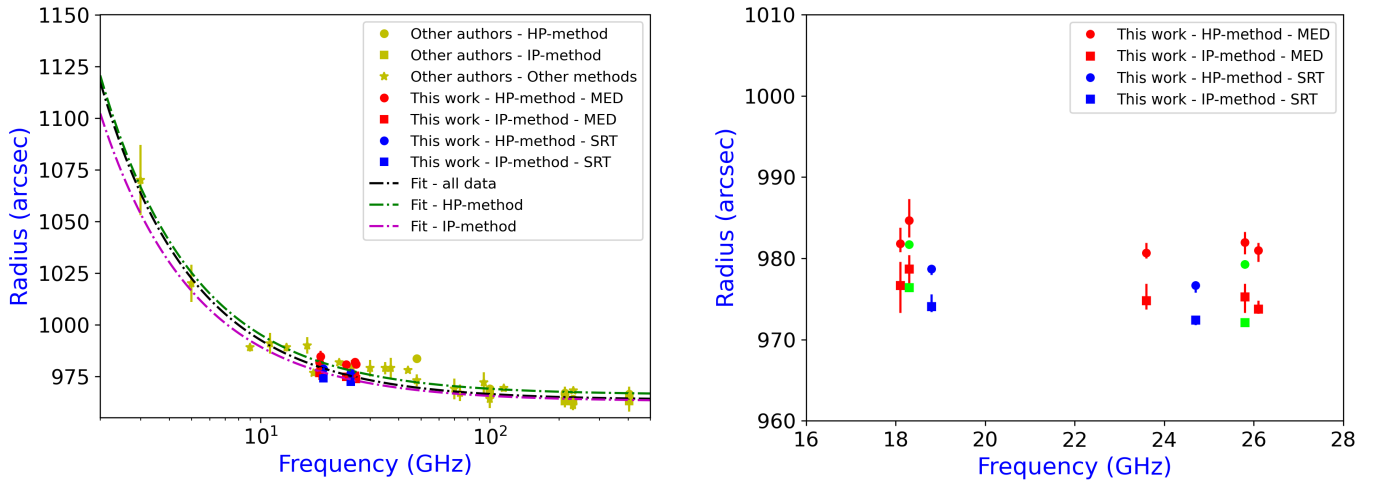


**Fig. 9.** Left: Solar radius as a function of frequency, with our measures of  $R_c$  obtained through the modelling; the dashed lines represent the fitted exponential trend (black: all data; green: HP-method; magenta: IP-method); the yellow points are previous measurements from other authors (see Table 1 in Menezes & Valio 2017; Menezes et al. 2022, and references therein), the circle and squared points are the present radius values derived from Grueff and SRT. Right: Plot with our measures of  $R_c$  obtained through the HP-method (circle points) and the IP-method (squared points). The green points indicate the measures of  $R_c$  obtained from the averaged solar maps of the Grueff Radio Telescope through the HP-method (circle points) and the IP-method (squared points).

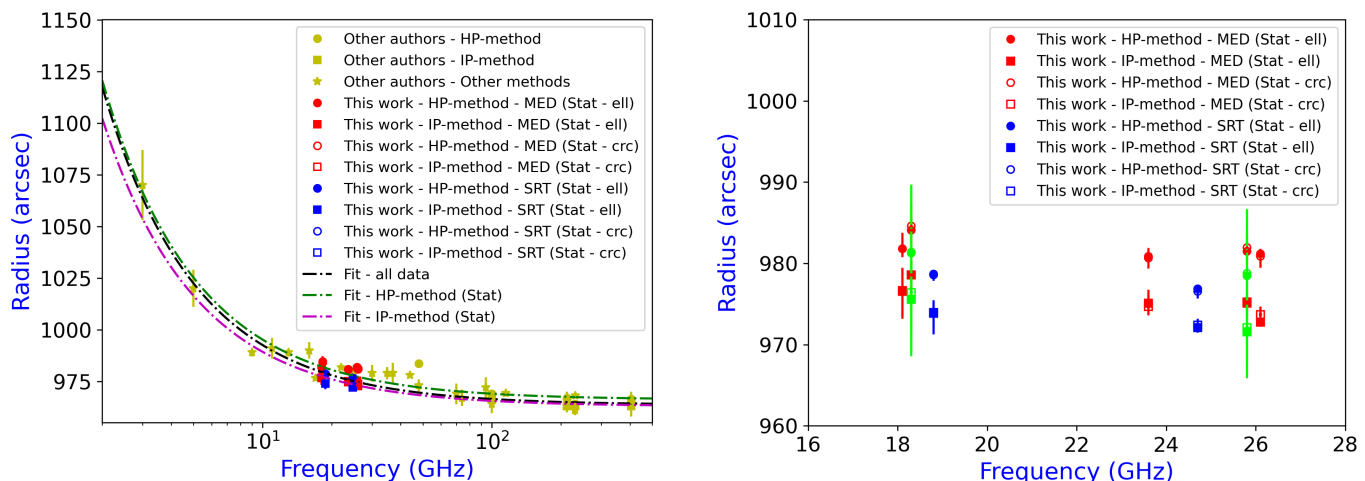


**Fig. 10.** Left: Solar radius as a function of frequency, with our measures of  $R_c$  obtained through the statistical approach; see the caption of Figure 9 for a full description of the colorbars and the symbols. Right: Plot with our measures of  $R_c$  obtained through the statistical approach.

$R_{eq}$  becomes greater than  $R_{pol}$ , suggesting the starting point of the rising phase of the 11-year solar activity cycle.

## 6. Conclusions and future developments

In this paper, we mainly focus on the first measurements of the solar radius carried out using the Medicina "Gavril Grueff" Radio Telescope and SRT – along with a comprehensive correlation analysis that also takes solar activity into account. Spanning a period of five years, from 2018 to mid-2023, we collected around 300 single-dish observations. This time frame covers approximately half of a solar cycle, and the observations were conducted in the radio K-band ranging between 18.1 GHz and 26.1 GHz. From the seven observing frequencies available during our solar sessions, we have specifically chosen four frequencies for our analysis. These selections were made based on their consistent time coverage. Precisely, we employed frequencies of 18.3 GHz and 25.8 GHz for observations at Medicina, and frequencies of 18.8 GHz and 24.7 GHz for observations at SRT. These chosen frequencies contribute significantly to a robust and meaningful analysis of our solar radius measurements. To assess the quality of our radius determinations in our solar maps, we analysed the role of the antenna beam pattern on these maps employing two 2D-models for solar emission convolved with accurate beam models, built adopting a Bayesian approach (ECB- and 2GECB-models).

The mean radii ( $R_c$ ,  $R_{eq}$ , and  $R_{pol}$ ) calculated among all our solar maps (for each observing frequency and radio telescope) – reported in Tables 1 and 2 – show values compatible with the ones reported in literature. Our measurements show a weak prolateness of the solar limb ( $R_{eq} > R_{pol}$ ), although  $R_{eq}$  and  $R_{pol}$  are compatible within  $3\sigma$  errors. In particular, the radii calculated with the HP-method and the ECB-model are larger than those measured through the IP-method and the 2GECB-model. Moreover, while the HP-method seems to be independent of the antenna beam pattern, future observations of the Sun at SRT will allow us to clarify whether the IP-method is also independent of the antenna beam pattern.

As reported in Tables 4, 5 and 6, the 13-month running means applied to the solar radii measured at Medicina (18.3 and 25.8 GHz) and the sunspot index number indicate (1) a positive correlation between the 11-year solar activity cycle and the tem-

poral variation of both  $R_c$  and  $R_{eq}$  at all observing frequencies, and (2) an anti-correlation between the temporal variation of  $R_{pol}$  and the solar activity, especially at 25.8 GHz. Moreover, the time variation of  $R_{eq}$  and  $R_{pol}$  for the solar data of the Grueff Radio Telescope shows a positive correlation, especially at 18.3 GHz. Our results about the correlation analysis may indicate an agreement with the analysis presented in literature for similar radio frequencies.

The bump observed at the end of 2020 both in the radii and in the solar activity, especially at 18.3 GHz, constrains the positive correlation between  $R_{\odot}$  and the solar activity at this observing frequency. At 25.8 GHz, the time evolution of  $R_{\odot}$  obtained using the ECB- and 2GECB-models shows that the bump in the solar activity corresponds to the time when  $R_{eq}$  becomes greater than  $R_{pol}$ , suggesting the starting point of the rising phase of the solar activity cycle.

Our results show that specific procedures for the  $R_{\odot}$  measurement, suited for the modelling of both the behaviour of the solar disk and the coronal emission (such as the case of the IP-method and the 2GECB-model), result in a lower bias in solar radius determination (and hence in a smaller value of  $R_{\odot}$ ) and in the detection of anti-correlation between the temporal variation of  $R_{pol}$  and the solar activity. This aspect suggests that the IP-method, and especially the 2GECB-model, could be among the most physically reliable methods for the calculation of  $R_{\odot}$  and its variation over time. Moreover, the radii obtained with the 2GECB-model range between the values obtained with the specific theoretical atmospheric models and the HP/IP-methods, suggesting that a non-negligible coronal emission level causes the decrease of the radius. We will discuss this aspect in a separate paper (Marongiu et al. 2023).

Future observations and detailed theoretical analysis with the Grueff Radio Telescope and SRT – for longer periods of time and in multi-frequency approach thanks also to new PON receivers at SRT operating up to 116 GHz – are crucial to better clarify several aspects, such as (1) the correlation between the solar activity and the solar size, (2) the polar and equatorial trends of the solar atmosphere, and (3) the question of the limb brightening (especially the presence of the polar brightening during the solar minima), which will be the subject of an upcoming work.

*Acknowledgements.* The Medicina radio telescope is funded by the Ministry of University and Research (MUR) and is operated as National Facility by the Na-

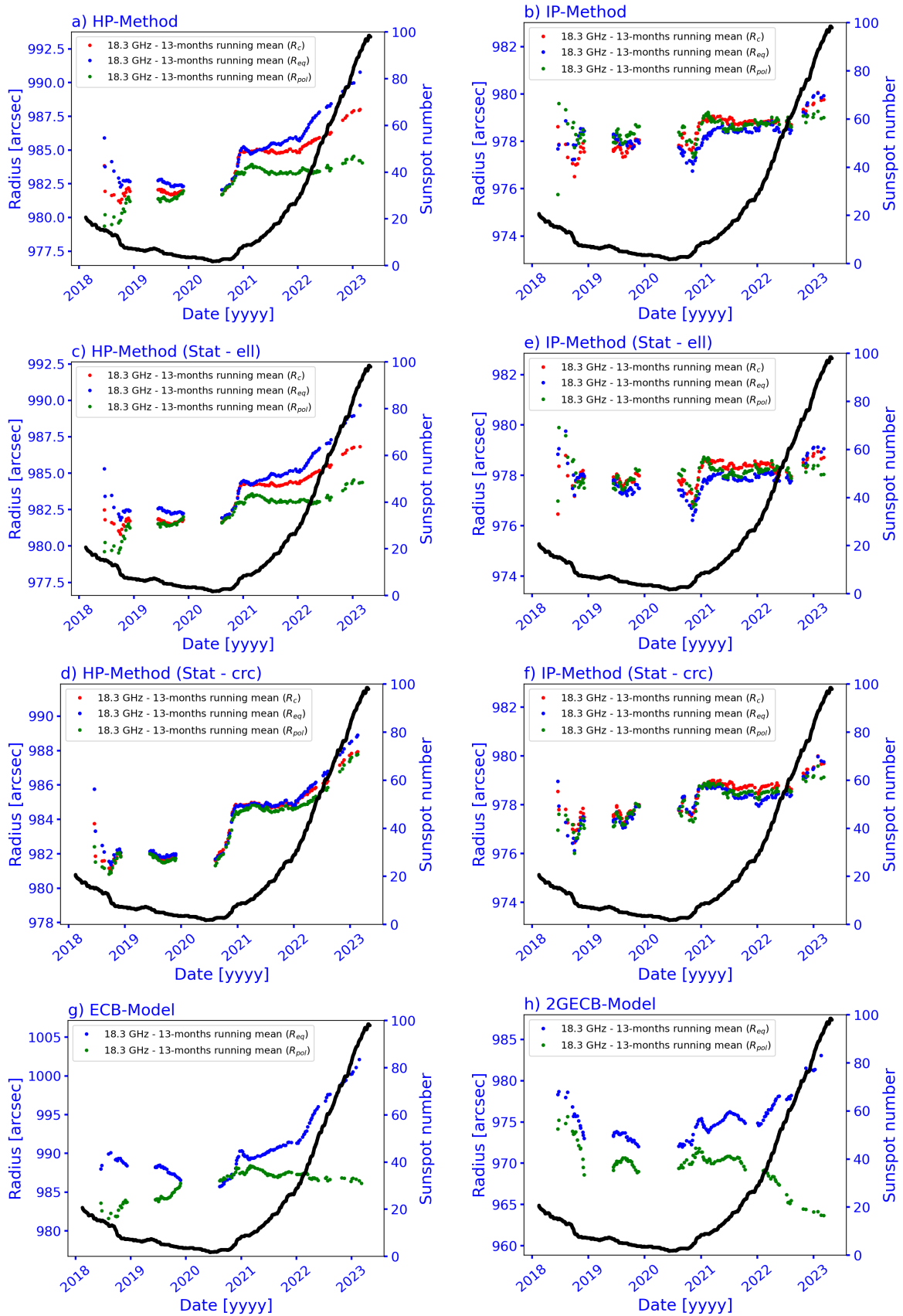


**Fig. 11.** 13-month running means applied at the solar radii obtained from the Grueff maps (18.3 GHz). Red points indicate  $R_c$ , blue points indicate  $R_{eq}$ , green points indicate  $R_{pol}$ , and black points indicate the sunspot index number. Plots (a) and (b) are referred to HP-method and IP-method, respectively; (c) and (d) are referred to HP-method and IP-method, respectively, for the elliptical-based statistical procedure; (e) and (f) are referred to HP-method and IP-method, respectively, for the circular-based statistical procedure; (g) and (h) are referred to ECB- and 2GECB-models, respectively.

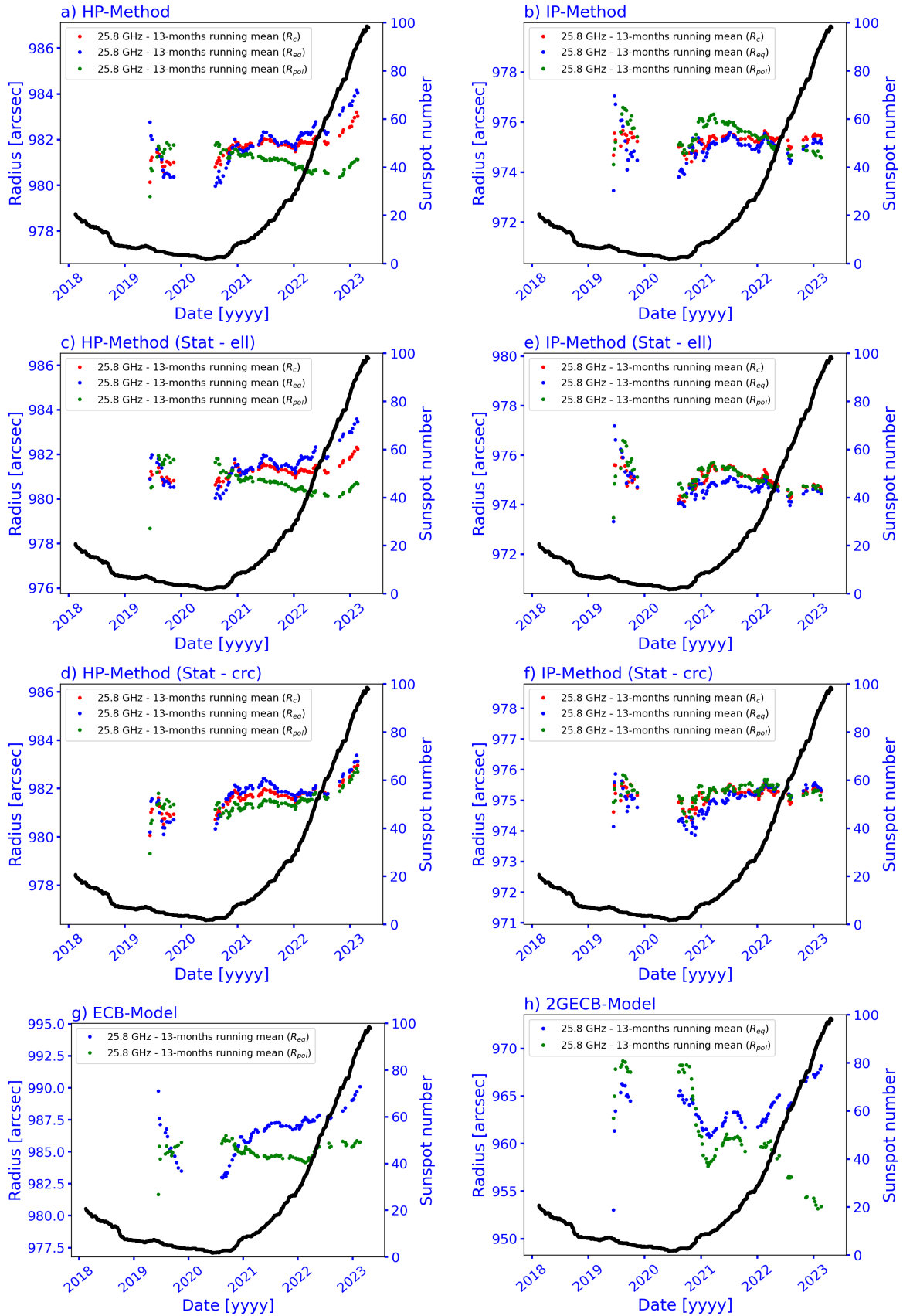


**Fig. 12.** 13-month running means applied at the solar radii obtained from the Grueff maps (25.8 GHz). Red points indicate  $R_c$ , blue points indicate  $R_{eq}$ , green points indicate  $R_{poi}$ , and black points indicate the sunspot index number. See the caption of Fig. 11 for a full description of the plots.



tional Institute for Astrophysics (INAF). The Sardinia Radio Telescope is funded by the Ministry of University and Research (MUR), Italian Space Agency (ASI), and the Autonomous Region of Sardinia (RAS) and is operated as National Facility by the National Institute for Astrophysics (INAF). The Enhancement of the Sardinia Radio Telescope (SRT) for the study of the Universe at high radio frequencies is financially supported by the National Operative Program (Programma Operativo Nazionale - PON) of the Italian Ministry of University and Research "Research and Innovation 2014-2020", Notice D.D. 424 of 28/02/2018 for the granting of funding aimed at strengthening research infrastructures, in implementation of the Action II.1 – Project Proposal PIR01\_00010. We acknowledge the Computing Centre at INAF - Istituto di Radioastronomia for providing resources and staff support during the processing of solar data presented in this paper.

## ORCID iDs

M. Marongiu: <https://orcid.org/0000-0002-5817-4009>  
 A. Pellizzoni: <https://orcid.org/0000-0002-4590-0040>  
 S. Mulas: <https://orcid.org/0000-0002-5455-1233>  
 S. Righini: <https://orcid.org/0000-0001-7332-5138>  
 R. Nesti: <https://orcid.org/0000-0003-0303-839X>  
 G. Murtas: <https://orcid.org/0000-0002-7836-7078>  
 E. Egron: <https://orcid.org/0000-0002-1532-4142>  
 M. N. Iacolina: <https://orcid.org/0000-0003-4564-3416>  
 A. Melis: <https://orcid.org/0000-0002-6558-1315>  
 G. Valente: <https://orcid.org/0000-0003-1197-9050>  
 G. Serra: <https://orcid.org/0000-0003-0720-042X>  
 S. L. Guglielmino: <https://orcid.org/0000-0002-1837-2262>  
 A. Zanichelli: <https://orcid.org/0000-0002-2893-023X>  
 P. Romano: <https://orcid.org/0000-0001-7066-6674>  
 S. Loru: <https://orcid.org/0000-0001-5126-1719>  
 M. Bachetti: <https://orcid.org/0000-0002-4576-9337>  
 A. Bemporad: <https://orcid.org/0000-0001-5796-5653>  
 F. Buffa: <https://orcid.org/0000-0001-9256-4476>  
 R. Concu: <https://orcid.org/0000-0003-3621-349X>  
 G. L. Deiana: <https://orcid.org/0000-0002-5404-5162>  
 C. Karakotia: <https://orcid.org/0009-0002-9669-7692>  
 A. Ladu: <https://orcid.org/0000-0003-1920-9560>  
 A. Maccaferri: <https://orcid.org/0000-0001-7231-4007>  
 P. Marongiu: <https://orcid.org/0000-0003-0314-7801>  
 M. Messerotti: <https://orcid.org/0000-0002-5422-1963>  
 A. Navarrini: <https://orcid.org/0000-0002-6191-6958>  
 A. Orfei: <https://orcid.org/0000-0002-8723-5093>  
 P. Ortu: <https://orcid.org/0000-0002-2644-2988>  
 M. Pili: <https://orcid.org/0000-0003-3715-1091>  
 T. Pisanu: <https://orcid.org/0000-0003-2510-7501>  
 G. Pupillo: <https://orcid.org/0000-0003-2172-1336>  
 A. Saba: <https://orcid.org/0000-0002-1607-5010>  
 L. Schirru: <https://orcid.org/0000-0002-8199-6510>  
 C. Tiburzi: <https://orcid.org/0000-0001-6651-4811>  
 P. Zucca: <https://orcid.org/0000-0002-6760-797X>

## References

Alissandrakis, C. E., Patsourakos, S., Nindos, A., & Bastian, T. S. 2017, *A&A*, 605, A78  
 Antia, H. M. 1998, *A&A*, 330, 336  
 Aschwanden, M. J. 2004, *Physics of the Solar Corona. An Introduction*  
 Auchere, F., Boulade, S., Koutchmy, S., et al. 1998, *A&A*, 336, L57  
 Bachurin, A. F. 1983, *Izvestiya Ordena Trudovogo Krasnogo Znameni Krymskoj  
 Astrofizicheskoy Observatorii*, 68, 68  
 Belkora, L., Hurford, G. J., Gary, D. E., & Woody, D. P. 1992, *ApJ*, 400, 692  
 Bolli, P., Orlati, A., Stringhetti, L., et al. 2015, *Journal of Astronomical Instru-  
 mentation*, 04, 1550008

Brown, R. L., Wild, W., & Cunningham, C. 2004, *Advances in Space Research*, 34, 555  
 Bush, R. I., Emilio, M., & Kuhn, J. R. 2010, *ApJ*, 716, 1381  
 Chapman, G. A., Dobias, J. J., & Walton, S. R. 2008, *ApJ*, 681, 1698  
 Chauvenet, W. 1863, *A manual of spherical and practical astronomy*  
 Coates, R. J. 1958, *ApJ*, 128, 83  
 Costa, J. E. R., Homor, J. L., & Kaufmann, P. 1986, in *Solar Flares and Coronal  
 Physics Using P/OF as a Research Tool*, 201–207  
 Costa, J. E. R., Silva, A. V. R., Makhmutov, V. S., et al. 1999, *ApJ*, 520, L63  
 Dansgaard, W., Johnsen, S. J., Reeh, N., et al. 1975, *Nature*, 255, 24  
 Delaboudinière, J. P., Artzner, G. E., Brunaud, J., et al. 1995, *Sol. Phys.*, 162, 291  
 Delmas, C. & Laclare, F. 2002, *Sol. Phys.*, 209, 391  
 Dziembowski, W. A., Goode, P. R., & Schou, J. 2001, *ApJ*, 553, 897  
 Egidì, A., Caccin, B., Sofia, S., et al. 2006, *Sol. Phys.*, 235, 407  
 Egron, E., Vacca, V., Carboni, G., et al. 2022, *SRT performance measurements  
 (2018-2021)*, Tech. Rep. 178, OA@INAF  
 Emilio, M., Couvidat, S., Bush, R. I., Kuhn, J. R., & Scholl, I. F. 2015, *ApJ*, 798, 48  
 Emilio, M., Kuhn, J. R., Bush, R. I., & Scherrer, P. 2000, *ApJ*, 543, 1007  
 Emilio, M., Kuhn, J. R., Bush, R. I., & Scholl, I. F. 2012, *ApJ*, 750, 135  
 Fontenla, J. M., Avrett, E. H., & Loeser, R. 1993, *ApJ*, 406, 319  
 Foreman-Mackey, D., Hogg, D. W., Lang, D., & Goodman, J. 2013, *PASP*, 125, 306  
 Fuerst, E., Hirth, W., & Lantos, P. 1979, *Sol. Phys.*, 63, 257  
 Gilliland, R. L. 1981, *ApJ*, 248, 1144  
 Giménez de Castro, C. G., Pereira, A. L. G., Valle Silva, J. F., et al. 2020, *ApJ*, 902, 136  
 Giménez de Castro, C. G., Varela Saraiva, A. C., Costa, J. E. R., & Selhorst, C. L. 2007, *A&A*, 476, 369  
 Gleissberg, W. 1966, *Journal of the British Astronomical Association*, 76, 265  
 Gough, D. 2001, *Nature*, 410, 313  
 Govoni, F., Bolli, P., Buffa, F., et al. 2021, in *2021 XXXIVth General Assembly  
 and Scientific Symposium of the International Union of Radio Science (URSI  
 GASS)*, 1–4  
 Haberreiter, M., Schmutz, W., & Kosovichev, A. G. 2008, *ApJ*, 675, L53  
 Hiremath, K. M. & Mandi, P. I. 2004, *New A*, 9, 651  
 Hiremath, K. M., Manjunath, H., & Soon, W. 2015, *New A*, 35, 8  
 Horne, K., Hurford, G. J., Zirin, H., & de Graauw, T. 1981, *ApJ*, 244, 340  
 Jones, E., Oliphant, T., Peterson, P., et al. 2001–, *SciPy: Open source scientific  
 tools for Python*, [Online; accessed <today>]  
 Kaufmann, P., Parada, N. J., Magun, A., et al. 1994, in *Proceedings of Kofu  
 Symposium*, 323–326  
 Kilic, H. & Golbasi, O. 2011, *Ap&SS*, 334, 75  
 Konz, N. & Reichart, D. E. 2023, *arXiv e-prints*, arXiv:2301.07838  
 Kosovichev, A. & Rozelot, J.-P. 2018, *ApJ*, 861, 90  
 Kosugi, T., Ishiguro, M., & Shibasaki, K. 1986, *PASJ*, 38, 1  
 Kuhn, J. R., Bush, R. I., Emilio, M., & Scherrer, P. H. 2004, *ApJ*, 613, 1241  
 Laclare, F., Delmas, C., Coin, J. P., & Irbah, A. 1996, *Sol. Phys.*, 166, 211  
 Landi, E. & Chiuderi Drago, F. 2008, *ApJ*, 675, 1629  
 Landi Degl'Innocenti, E. 2007, *Fisica Solare*, ISSN 2038-5714 (Springer Mi-  
 lano)  
 Lindsey, C., Hildebrand, R. H., Keene, J., & Whitcomb, S. E. 1981, *ApJ*, 248, 830  
 Mamajek, E. E., Prsa, A., Torres, G., et al. 2015, *arXiv e-prints*,  
 arXiv:1510.07674  
 Maples, M. P., Reichart, D. E., Konz, N. C., et al. 2018, *ApJS*, 238, 2  
 Marongiu, M., Pellizzoni, A., Bachetti, M., et al. 2022, *A dedicated pipeline to  
 analyse solar data with INAF radio telescopes: SUNPIT (SUNdish PIpeLine  
 Tool)*, Tech. Rep. 137, OA@INAF  
 Marongiu, M., Pellizzoni, A., et al. 2023, *A&A*, submit.  
 Marongiu, M., Pellizzoni, A. P., Mulas, S., & Murtas, G. 2021, *A Python ap-  
 proach for solar data analysis: SUNDARA (SUNdish Active Region Anal-  
 yser)*, preliminary development, Tech. Rep. 81, OA@INAF  
 Meftah, M., Corbard, T., Hauchecorne, A., et al. 2018, *A&A*, 616, A64  
 Meftah, M., Corbard, T., Irbah, A., et al. 2014, *A&A*, 569, A60  
 Melis, A., Concu, R., Trois, A., et al. 2018, *Journal of Astronomical Instrumen-  
 tation*, 7, 1850004  
 Melnik, V. N., Shepelev, V. A., Poedts, S., et al. 2018, *Sol. Phys.*, 293, 97  
 Menezes, F., Selhorst, C. L., Giménez de Castro, C. G., & Valio, A. 2021, *ApJ*, 910, 77  
 Menezes, F., Selhorst, C. L., Giménez de Castro, C. G., & Valio, A. 2022, *MN-  
 RAS*, 511, 877  
 Menezes, F. & Valio, A. 2017, *Sol. Phys.*, 292, 195  
 Mercier, C. & Chambe, G. 2015, *A&A*, 583, A101  
 Mulas, S., Pellizzoni, A., Iacolina, N. M., et al. 2022, *A New Method for Accu-  
 rate Calibration of Solar Disk Emission in the Radio Band*, Tech. rep.  
 Nakajima, H., Nishio, M., Enome, S., et al. 1994, *IEEE Proceedings*, 82, 705  
 Nakajima, H., Nishio, M., Enome, S., et al. 1995, *Journal of Astrophysics and  
 Astronomy Supplement*, 16, 437

- Neckel, H. 1995, *Sol. Phys.*, 156, 7
- Nindos, A., Kundu, M. R., White, S. M., et al. 1999, *ApJ*, 527, 415
- Noël, F. 2004, *A&A*, 413, 725
- Pellizzoni, A., Righini, S., Iacolina, M. N., et al. 2022, *Sol. Phys.*, 297, 86
- Pellizzoni, A., Righini, S., Murtas, G., et al. 2019, *Nuovo Cimento C Geophysics Space Physics C*, 42, 9
- Pelyushenko, S. A. & Chernyshev, V. I. 1983, *Soviet Ast.*, 27, 340
- Plainaki, C., Antonucci, M., Bemporad, A., et al. 2020, *Journal of Space Weather and Space Climate*, 10, 6
- Prandoni, I., Murgia, M., Tarchi, A., et al. 2017, *A&A*, 608, A40
- Prša, A., Harmanec, P., Torres, G., et al. 2016, *AJ*, 152, 41
- Qu, Z. N. & Xie, J. L. 2013, *ApJ*, 762, 23
- Quaglia, L., Irwin, J., Emmanouilidis, K., & Pessi, A. 2021, *ApJS*, 256, 36
- Ramesh, R., Nataraj, H. S., Kathiravan, C., & Sastry, C. V. 2006, *ApJ*, 648, 707
- Reis Neto, E., Andrei, A. H., Penna, J. L., Jilinski, E. G., & Puliaev, S. P. 2003, *Sol. Phys.*, 212, 7
- Ribes, E., Beardsley, B., Brown, T. M., et al. 1991, in *The Sun in Time*, ed. C. P. Sonett, M. S. Giampapa, & M. S. Matthews, 59
- Ribes, E., Merlin, P., Ribes, J. C., & Bartholot, R. 1989, *Annales Geophysicae*, 7, 321
- Ribes, E., Ribes, J. C., & Bartholot, R. 1987, *Nature*, 326, 52
- Rozelot, J. P. 1998, *Sol. Phys.*, 177, 321
- Rozelot, J. P., Kosovichev, A., & Kilcik, A. 2015, *ApJ*, 812, 91
- Rozelot, J. P., Kosovichev, A. G., & Kilcik, A. 2018, in *Variability of the Sun and Sun-Like Stars: from Asteroseismology to Space Weather*, ed. J. P. Rozelot & E. S. Babayev, 89–99
- Secchi, P. A. 1872, *MNRAS*, 32, 226
- Selhorst, C. L., Giménez de Castro, C. G., Válio, A., Costa, J. E. R., & Shibasaki, K. 2011, *ApJ*, 734, 64
- Selhorst, C. L., Kallunki, J., Giménez de Castro, C. G., Valio, A., & Costa, J. E. R. 2019a, *Sol. Phys.*, 294, 175
- Selhorst, C. L., Silva, A. V. R., & Costa, J. E. R. 2004, *A&A*, 420, 1117
- Selhorst, C. L., Silva, A. V. R., & Costa, J. E. R. 2005, *A&A*, 433, 365
- Selhorst, C. L., Silva, A. V. R., Costa, J. E. R., & Shibasaki, K. 2003, *A&A*, 401, 1143
- Selhorst, C. L., Simões, P. J. A., Brajša, R., et al. 2019b, *ApJ*, 871, 45
- Sharma, S. 2017, *ARA&A*, 55, 213
- Shibasaki, K. 1998, in *Astronomical Society of the Pacific Conference Series*, Vol. 140, *Synoptic Solar Physics*, ed. K. S. Balasubramaniam, J. Harvey, & D. Rabin, 373
- Simon, M. & Zirin, H. 1969, *Sol. Phys.*, 9, 317
- Sofia, S., Dunham, D. W., Dunham, J. B., & Fiala, A. D. 1983, *Nature*, 304, 522
- Stuiver, M. 1980, *Nature*, 286, 868
- Swanson, P. N. 1973, *Sol. Phys.*, 32, 77
- Ulrich, R. K. & Bertello, L. 1995, *Nature*, 377, 214
- van Haarlem, M. P., Wise, M. W., Gunst, A. W., et al. 2013, *A&A*, 556, A2
- Vaquero, J. M., Svalgaard, L., Carrasco, V. M. S., et al. 2016, *Sol. Phys.*, 291, 3061
- Vernazza, J. E., Avrett, E. H., & Loeser, R. 1981, *ApJS*, 45, 635
- Wilson, T. L., Rohlf, K., & Hüttemeister, S. 2013, *Tools of Radio Astronomy*
- Withbroe, G. L. 1970, *Sol. Phys.*, 11, 42
- Wittmann, A. D., Alge, E., & Bianda, M. 1993, *Sol. Phys.*, 145, 205
- Wrixon, G. T. 1970, *Nature*, 227, 1231
- Zhang, P., Zucca, P., Kozarev, K., et al. 2022, *ApJ*, 932, 17